Authigenic 10Be/9Be ratio signature of the Matuyama-Brunhes boundary in the Montalbano Jonico marine succession

Quentin Simon, Didier Bourles, Franck Bassinot, Sébastien Nomade, Maria Marino, Neri Ciaranfi, Angela Girone, Patrizia Maiorano, Nicolas Thouveny, Sandrine Choy, et al.

Earth and Planetary Science Letters 460 (2017) 255–267

Contents lists available at ScienceDirect

Earth and Planetary Science Letters

www.elsevier.com/locate/epsl

Authigenic $^{10}Be/^{9}Be$ ratio signature of the Matuyama–Brunhes boundary in the Montalbano Jonico marine succession

Quentin Simon [a,b,*], Didier L. Bourlès [a], Franck Bassinot [c], Sébastien Nomade [c], Maria Marino [d], Neri Ciaranfi [d], Angela Girone [d], Patrizia Maiorano [d], Nicolas Thouveny [a], Sandrine Choy [a,b], Fabien Dewilde [c], Vincent Scao [c], Gulay Isguder [c], Dominique Blamart [c], ASTER Team [a,1]

[a] CEREGE UM34, Aix Marseille Univ, CNRS, IRD, Coll France, Aix en Provence, France
[b] IPGP, Université Paris Diderot, Sorbonne Paris-Cité, UMR 7154 CNRS, 75238 Paris, France
[c] Laboratoire des Sciences du Climat et de L'Environnement, UMR8212, LSCE/IPSL, CEA-CNRS-UVSQ and Université Paris-Saclay, Gif-Sur-Yvette, France
[d] Department of Earth and Geoenvironmental Science, University of Bari Aldo Moro, E. Orabona 4, 70125 Bari, Italy

ARTICLE INFO

Article history:
Received 2 August 2016
Received in revised form 8 November 2016
Accepted 28 November 2016
Available online 15 December 2016
Editor: M. Frank

Keywords:
^{10}Be cosmogenic nuclide
authigenic $^{10}Be/^{9}Be$ ratio
Matuyama–Brunhes Boundary (MBB)
high-resolution oxygen isotope stratigraphy
MIS 19
GSSP stratotype

ABSTRACT

Geomagnetic dipole moment (GDM) lows associated with polarity reversals or geomagnetic excursions induce significant modulation of the cosmogenic nuclide Beryllium-10 (^{10}Be) production. Hence, the reconstruction of atmospheric ^{10}Be production rates from natural archives such as marine sedimentary sequences or ice cores constitutes a complementary approach, independent from paleomagnetic measurements, to decipher past GDM fluctuations. This is particularly important in the Montalbano Jonico succession (South Italy) since it is candidate to host the Global Stratotype Section and Point of the Middle Pleistocene Stage but where the magnetostratigraphic positioning of the Matuyama–Brunhes boundary (MBB) has not been available up to now. This study presents (1) original authigenic ^{10}Be cosmogenic nuclide and ^{9}Be stable isotope results, and (2) new high-resolution benthic oxygen isotope record covering termination IX and Marine Isotope Stage (MIS) 19. A robust chronological framework is established on the basis of (i) our oxygen isotope stratigraphy, using the strong analogies between MIS 1 and MIS 19c in terms of orbital forcing and CO_2 level, and (ii) one precise $^{40}Ar/^{39}Ar$ date obtained in the tephra layer V4. The authigenic $^{10}Be/^{9}Be$ ratio record marks the atmospheric ^{10}Be overproduction linked to the dipole low accompanying the MBB transition, with a characteristic twofold increase of the ^{10}Be production at the end of MIS 19c and early MIS 19b. This signature is similar to those described in both marine and ice core records. The detailed chronostratigraphy constrained by a radiometrically-dated tephra layer (773.9 ± 1.3 ka) within the MBB interval, makes it possible to discuss the structure and to assess the timing of the ^{10}Be-production changes, and thus the MBB geomagnetic variations, with an unprecedented accuracy for a marine archive (sedimentation rates ~80 cm/ka). These new cosmogenic nuclide production signatures provide the only missing constraint required for retaining the Montalbano Jonico succession as a global-scale correlation reference section for the Early–Middle Pleistocene boundary.

1. Introduction

The identification of the most recognizable chronostratigraphic marker in weathered continental deposits and in marine sedimentary sequences: the Matuyama–Brunhes boundary (MBB), the last geomagnetic reversal, is a primary criterion for defining the Early–Middle Pleistocene boundary. Along with paleomagnetic measurements, analysis of the meteoric cosmogenic radionuclide beryllium-10 (^{10}Be) in natural archives provides robust information on the geomagnetic dipole moment (GDM) variations through a non-linear inverse relationship between its atmospheric production rate and the Earth magnetic field variability (e.g. Masarik and Beer, 2009). The ^{10}Be nuclides are produced in the atmosphere by spallation reactions between highly energetic primary (mainly protons (H^{+}) and alpha particles ($^{4}He^{2+}$)) and secondary (mainly neutrons) galactic cosmic ray particles and atmospheric

* Corresponding author.
E-mail address: simon@cerege.fr (Q. Simon).
[1] Georges Aumaître, Karim Keddadouche.

http://dx.doi.org/10.1016/j.epsl.2016.11.052
0012-821X/

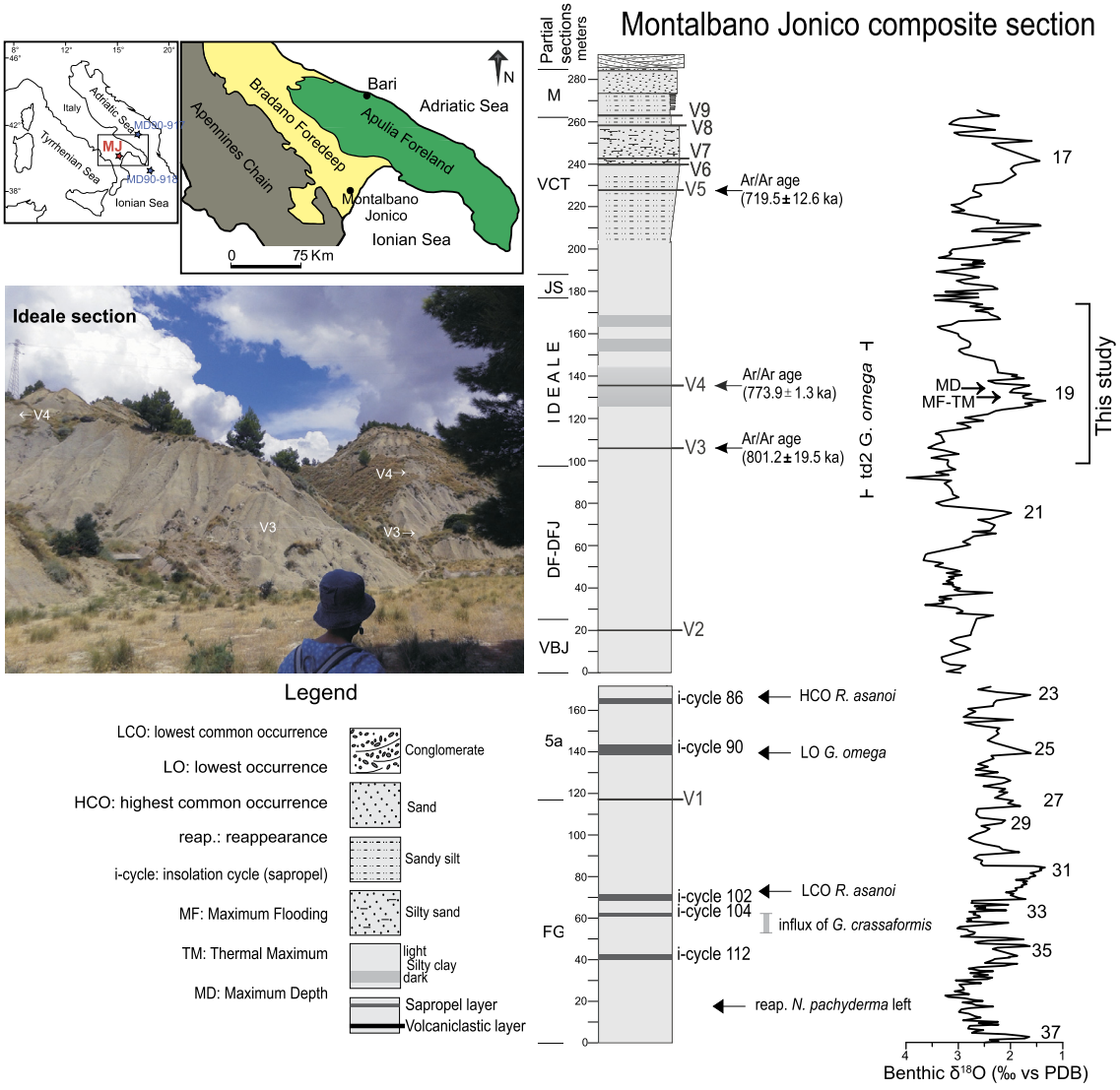

Fig. 1. Location and lithostratigraphy of the Montalbano Jonico succession (MJS). Main lithological features of the composite section obtained by correlating several partial sections (FG-M). Chrono-biostratigraphic constraints are shown on the right together with the benthic $\delta^{18}O$ record (Ciaranfi et al., 2010; Maiorano et al., 2010; Girone et al., 2013). Marine Isotope Stages are according to Ciaranfi et al. (2010). A photo of the Ideale section including the V3 and V4 tephra layers and the location of core MD90-917 and MD90-918 used for the age model comparison (see section 5) are also presented on the left hand-side.

nitrogen and oxygen atoms (Lal and Peters, 1967). The penetration rate of these primary galactic cosmic ray particles into the atmosphere varies with latitude as a function of the vertical cut-off rigidity, which quantifies the ability of charged particles to penetrate the geomagnetic field lines. Thus, large ^{10}Be-production increases result from a low magnetospheric shielding due to weak GDM strength as demonstrated by numerous studies regarding geomagnetic excursions and reversals (e.g. Carcaillet et al., 2003; Muscheler et al., 2005; Raisbeck et al., 2006; Knudsen et al., 2008; Christl et al., 2010; Ménabréaz et al., 2012, 2014; Valet et al., 2014; Horiuchi et al., 2016; Simon et al., 2016a).

Since the Montalbano Jonico succession (MJS) is candidate to host the Global Stratotype Section and Point (GSSP) of the Middle Pleistocene, the clear recognition and precise positioning of the MBB are requisites because they condition the establishment of correlations at the global scale. Despite thoughtful stratigraphic and paleoenvironmental investigations that adequately satisfy most of the recommendations indicated for a global boundary stratotype, the MJS suffers from an unsuccessful attempt to obtain a reliable magnetostratigraphy (Sagnotti et al., 2010).

In order to satisfy this only missing criterion and provide a direct, reliable and comparable position of the MBB in the MJS, analyses of authigenic ^{10}Be and ^{9}Be isotope concentrations (i.e. fraction dissolved or chemically precipitated and adsorbed onto settling particles) were carried out in the Ideale section covering Marine Isotope Stages (MIS) 20–19 (Fig. 1). Normalization of the authigenic ^{10}Be cosmogenic nuclide by the authigenic ^{9}Be stable isotope released from continental weathering is mandatory in order to minimize the environmental disturbances (Bourlès et al., 1989) and compare authigenic ^{10}Be/^{9}Be ratio records with geomagnetic variability (see references above).

In this study, we present (1) original authigenic ^{10}Be/^{9}Be ratio results with an unprecedented accuracy for a marine archive given the very high sedimentation rate of the MJS through MIS 20–19, and (2) new high-resolution benthic oxygen isotope record (120–200 years resolution) from Termination IX (T.IX hereafter) to MIS 19a. In addition to the precise ^{40}Ar/^{39}Ar age of a tephra layer (i.e. V4), we use the orbital forcing and CO_2 level analogy between MIS 1 and MIS 19c to fine-tune the new $\delta^{18}O$ record to orbital oscillations and establish a robust chronological framework. We then conduct a comprehensive study of the structure of the

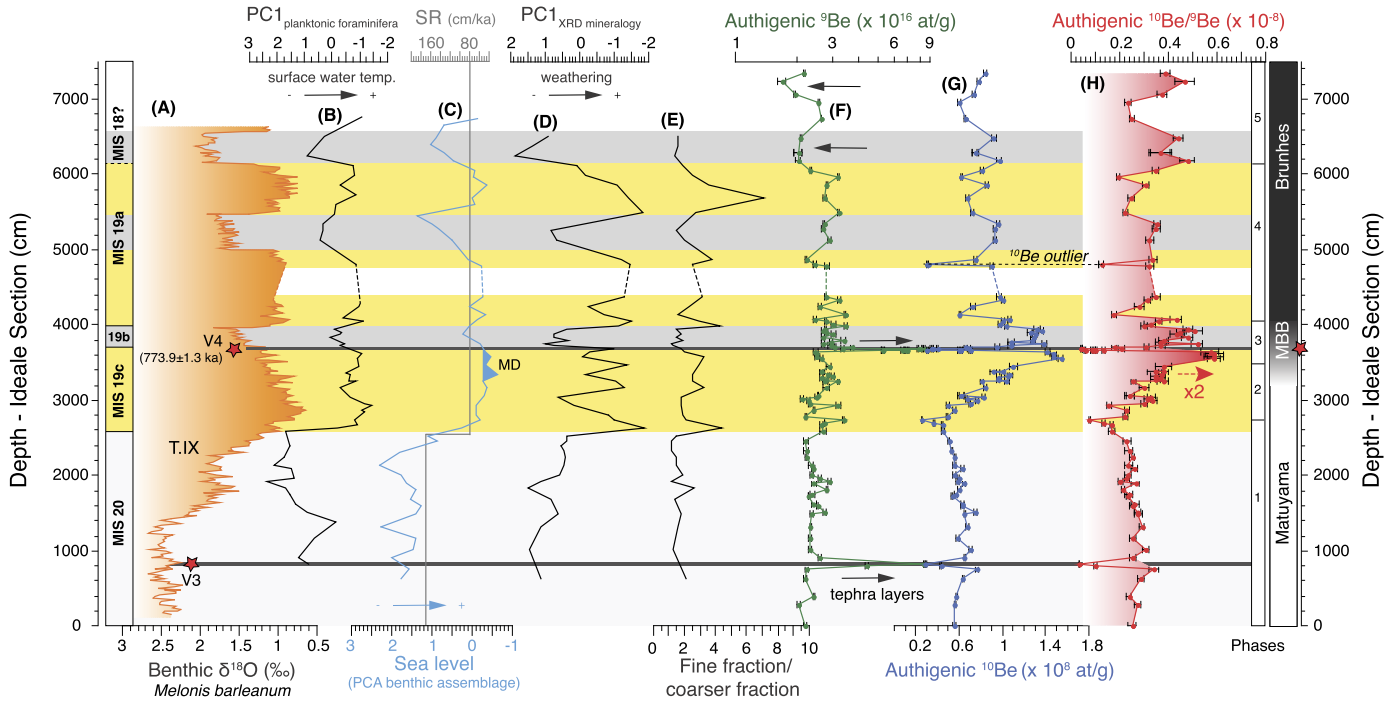

Fig. 2. Paleoenvironmental variations and authigenic beryllium isotopes results. (A) The oxygen isotope record from benthic foraminifera *Melonis barleanum* are expressed as $\delta^{18}O$ vs VPDB (‰). Principal component analyses of (B) planktonic foraminifera taxa, (D) XRD mineralogical content and (E) Fine fraction/coarser fraction ratio (0–8/>16 μm) are from Maiorano et al. (2016). (C) The relative sea level curve is derived from benthic foraminifera assemblages (Stefanelli, 2003). Maximum depth (MD) is highlighted in the figure. The sedimentation rate (SR, gray line) of the Ideale section is derived from the age model from this study (see section 5 and Fig. 4). (F) Authigenic ^{9}Be concentrations present two large spikes coeval with tephra layers V4 (3660 cm) and V3 (820 cm). The ^{10}Be (decay-corrected) concentrations (G) and authigenic $^{10}Be/^{9}Be$ ratios (H) present similar variations described in the text by distinct phases (from 1 to 5). These variations especially include a twofold increase within the 3550–3950 cm interval (phase 3) associated with the Matuyama–Brunhes Boundary (MBB). Paleoenvironmental proxies (A–E) yield clear distinction between Marine isotopic stage (MIS) 20, Termination IX (T.IX), and substages of MIS 19 (a–b–c). The red stars and black bars indicate the two tephra locations. (For interpretation of the references to color in this figure legend, the reader is referred to the web version of this article.)

authigenic $^{10}Be/^{9}Be$ ratio (proxy of atmospheric ^{10}Be production) changes within the new frame of the marine stable oxygen isotope stratigraphy, and discuss their timing and global correlation. This original study of the structure and chronology of the ^{10}Be production rate increase corresponding to the MBB in the Montalbano marine series constitutes a major prerequisite for geological time scale calibration.

2. Geological setting of the Montalbano Jonico Succession

The Montalbano Jonico succession (MJS) crops out in the Lucania Basin, a minor basin of the Bradano Foredeep (Bradano Trough, Casnedi, 1988) between the Apennines Chain and the Apulia Foreland (Fig. 1). The Bradano Trough was emplaced in the Early Pliocene and underwent significant modifications during the Late Pliocene and the Early Pleistocene. Its inner border moved northeastward while its outer margin spread gradually over the Apulia Foreland units (Casnedi et al., 1982). The MJS was deposited during the Early and Middle Pleistocene in an upper slope to inner shelf setting (Marino et al., 2015 and references therein). The whole section represents the regressive part of a third-order cycle with several fourth and fifth-order cycles mainly driven by climate changes (Ciaranfi et al., 2010).

The composite section of Montalbano Jonico, about 450 m thick, was reconstructed based on the study of several sections (FG-M, Fig. 1), that are well exposed along the left Agri River badland. It consists of upward coarsening deposits formed by hemipelagic silty clays and, in its upper part, by sandy silts to sands. Nine tephra layers (V1–V9) are interspersed in the MJS. They were chemically and mineralogically characterized and correlated to other tephra layers from south-central Italy lacustrine successions and marine sequences within a Lower–Middle Pleistocene Mediterranean tephrostratigraphic frame (Petrosino et al., 2015). The five sapropel horizons identified in the lower part of the section (Fig. 1) were correlated to insolation cycles i-112, i-104, i-102, i-90, and i-86, in agreement with the Mediterranean sapropel stratigraphy (Ciaranfi et al., 2010 and references therein). Stable oxygen isotope records (Fig. 1) combined with numerous biostratigraphical constraints (e.g. calcareous nannofossil, planktonic foraminifera) were used for astronomical calibration of the MJS, that covers the time interval between MIS 37 and MIS 16, i.e. 1.24 Ma to 0.64 Ma (Ciaranfi et al., 2010; Marino et al., 2015). The MJS represents a unique on-land continuous marine succession spanning such a long time interval and, together with the astronomically tuned Vrica section, covers the entire Calabrian Stage (Maiorano et al., 2010).

3. Environmental and lithological changes in the Ideale section

As part of the composite succession, the Ideale section is the one straddling MIS 19 within the Interval B of the MJS (Fig. 1), and is candidate to host the GSSP of the Middle Pleistocene (Head and Gibbard, 2015). This 73.5 m thick section consists of dark-light grey silty clays with intercalated tephra layers V3 and V4. High resolution multidisciplinary studies demonstrated the occurrence of glacial–interglacial phases and of rapid cooling/drying episodes indicating (sub)millennial-scale climate variability during T.IX and over MIS 19 (Bertini et al., 2015; Maiorano et al., 2016). The MIS 19 climatic variability is expressed by the large occurrence of halophyte and steppe taxa in the Ideale section during MIS 19b, while MIS 19a and 19c are rather characterized by woody and moderate herbaceous taxa (Maiorano et al., 2016). Enhanced chemical weathering has also been proved to develop in the neighboring area during warmer and wetter conditions characterizing the MIS

19 interval, as indicated by the principal component analysis performed on the mineralogical assemblage (Fig. 2D) and specifically by a prominent increase of the kaolinite content (Maiorano et al., 2016). Grain size variations (Fig. 2E) observed through the section also match climate phases with increased supply of finer grain size fraction (mainly clay <4 μm and fine silt at the expense of coarser silt and sand) into the basin, reflecting the existence of climate-induced transgressive/regressive phases (Maiorano et al., 2016). Investigations of macroinvertebrate palaeocommunities (D'Alessandro et al., 2003) and benthic foraminifera (Stefanelli et al., 2005) indicate inner to outer shelf environments with sporadic transition to upper slope. The relative paleodepth varies from about 100 m to 200 m between MIS 20 and 19 (Aiello et al., 2015) with a large relative sea level (RSL) rise corresponding to T.IX and a maximum depth in MIS 19c (Fig. 2C; D'Alessandro et al., 2003). Two RSL drops are observed along with major climatic changes during the MIS 19a oscillations, while minor RSL variations are observed during MIS 19c–b (Fig. 2C).

4. Materials and methods

The Ideale section (Fig. 1) has been sampled every 20-cm from fresh outcrops after removing the uppermost 10 cm surface layer. A short interval in the upper part of the section has not been sampled due to vegetation covering (Fig. 2). The depth scale used in this study is relative to the base of the Ideale section, set as the origin, i.e. 0 cm, that presents an unambiguous stratigraphic marker easily identified in the field (ground level at the base of the outcrop, see photo in Fig. 1).

The authigenic beryllium isotope analyses were carried out on 103 samples, with variable resolution (from 10 to 280 cm), at the CEREGE National Cosmogenic Nuclides Laboratory (France) according to the chemical procedure established by Bourlès et al. (1989) and summarized by Simon et al. (2016b). The natural authigenic ^{9}Be concentrations were measured using a graphite-furnace Atomic Absorption Spectrophotometer (AAS) with a double beam correction (Thermo Scientific ICE 3400®). The associated uncertainties (2σ) based on the reproducibility of quadruplicated measurements and the least-square fitting between measured absorbance at each stages of the standard-addition method vary around average values of 1.8%. The natural authigenic ^{10}Be concentration measurements were performed at the French AMS national facility ASTER (CEREGE). ^{10}Be sample concentrations are calculated from the measured spiked ^{10}Be/^{9}Be ratios normalized to the BeO STD-11 in-house standard ($1.191 \pm 0.013 \times 10^{-11}$; Braucher et al., 2015), and are decay-corrected using the ^{10}Be half-life ($T_{1/2}$) of 1.387 ± 0.012 Ma (Chmeleff et al., 2010; Korschinek et al., 2010). The precision (from statistical and instrumental uncertainties) of the measured ^{10}Be/^{9}Be ratios at the AMS varies around an average value of 2.1%. The uncertainties (2σ) of the calculated authigenic ^{10}Be/^{9}Be ratios are derived from analytical error propagation and vary around an average value of 5.6% (Table 1).

For oxygen stable isotopic stratigraphy, sediments were sampled from 150 to 6,630 cm, at a ~20 cm interval resolution, representing a total of 322 samples. Stable isotopic compositions were measured on the benthic foraminifera *Melonis barleanum* tests picked in the 315–355 μm size fractions. The analyses were performed on a GV-Isoprime dual-inlet gas mass spectrometer at LSCE laboratory. All results are expressed as δ^{18}O vs VPDB (in ‰) with respect to NBS 19 standard. The internal analytical reproducibility determined from replicate measurements of a carbonate standard is ±0.05% (1σ).

5. Results and interpretations

All authigenic ^{10}Be and ^{9}Be sample concentrations and corresponding ratios are listed in Table 1. The new δ^{18}O results presented in this study are listed in supplementary material (Table S1).

5.1. Authigenic ^{9}Be

The ^{9}Be concentrations vary between 1.7 and 8.4×10^{16} at/g (mean $= 3.03 \pm 1.37 \times 10^{16}$ at/g). High ^{9}Be concentration values reaching 8.4×10^{16} at/g, nearly fourfold higher than the average range, are found within, or immediately above, the V3 and V4 tephra layers (Table 1; Figs. 2F and 3A). These 5 and 10 cm thick layers, respectively, are composed of silty yellowish grey sediments with clayey matrix containing badly preserved pumice fragments (Petrosino et al., 2015) originating from pyroclastic eruptions of the Vulture stratovolcano (located 100 km northwest from the Montalbano Jonico area, Fig. 3A). Such unusual ^{9}Be-rich concentrations were only found within these two tephra layers suggesting direct inputs of easily soluble ^{9}Be that might be intrinsic in the tephra particles. Note that the distinct ^{9}Be concentration of the V5 tephra layer (Fig. 3A), located above the Ideale section (Fig. 1), and chemically close to the Campanian volcanic field products (Petrosino et al., 2015) could support a provenance influence.

No high ^{9}Be concentrations are observed prior to the tephra deposition, while high ^{9}Be values only span a limited 20 cm thick interval (Fig. 3B), most likely deposited within few years/decades following the V4 eruptive event. This supports: i) the low geochemical mobility behavior of Be isotopes once scavenged onto particles and deposited within the sedimentary column and, ii) the limited bioturbation mixing mainly due to very high sedimentation rates (Ciaranfi et al., 2010).

The authigenic ^{9}Be inputs associated with tephra layers V3 and V4 are related to direct mantle inputs and/or very dense particle environments following the fallout of pyroclastic flow, contributing to modify drastically the concentrations, scavenging rates and/or mixing of dissolved Be in the water column. Thus, it seems reasonable to exclude the tephra layers from the geomagnetic ^{10}Be/^{9}Be ratio interpretation given the peculiar geochemical behavior of dissolved Be isotopes within these specific intervals (Figs. 2F and 3).

Outside the tephra layers, ^{9}Be concentration variations are relatively stable throughout the record ranging from 1.7 to 3.5×10^{16} at/g, with an average value of $2.59 \pm 0.36 \times 10^{16}$ at/g. Two low ^{9}Be concentration values at 6,190–6,290 cm and 7,240 cm (Fig. 2F) correspond to major changes in detrital inputs (Fig. 2D–E) associated with the MIS 19a abrupt δ^{18}O oscillations or MIS 18 inception (Fig. 2A).

5.2. Authigenic ^{10}Be

The authigenic ^{10}Be (decay-corrected) concentrations vary from 0.26 to 1.54×10^{8} at/g with an average value of $0.77 \pm 0.30 \times 10^{8}$ at/g. In contrast with ^{9}Be variation, the ^{10}Be concentrations present clear fluctuations within the sequence, which can be grouped into five phases (Fig. 2G). From 0 to 2,730 cm depth (phase 1), the ^{10}Be concentrations have a mean value of $0.58 \pm 0.29 \times 10^{8}$ at/g and slightly decrease toward a minimum concentration of 0.26×10^{8} at/g at 2,730 cm. Then, the ^{10}Be concentrations increase rapidly to 1.10×10^{8} at/g at 3,455 cm depth (phase 2). Within the 3,550–3,950 cm interval (phase 3), the ^{10}Be concentrations are maximal with an average of $1.35 \pm 0.12 \times 10^{8}$ at/g, nearly doubling the average value of the prior interval (mean 0.67×10^{8} at/g). Inside that 500 cm thick layer, the 3,659–3,730 cm interval yields a significant drop in ^{10}Be concentration corresponding to sediments deposited immediately above the V4 tephra layer

Table 1
AMS measurements, authigenic ^{10}Be and ^{9}Be concentration and authigenic ^{10}Be/^{9}Be ratio of the Ideale section from the Montalbano Jonico succession.

Sample codes	Depth MJS composite (m)	Depth Ideale section (cm)	Age model (ka)	Sample weight [g]	Measured (^{10}Be/^{9}Be) $*10^{-11}$	Authigenic decay corrected ^{10}Be $*10^{8}$ [at·g^{-1}]	Authigenic ^{9}Be $*10^{16}$ [at·g^{-1}]	Authigenic ^{10}Be/^{9}Be $*10^{-8}$
v5	227.60	12990	657.3	1.0014	0.01 ± 0.000	0.04 ± 0.00	3.35 ± 0.07	0.01 ± 0.00
NC431	171.10	7340	727.9	1.0039	0.27 ± 0.005	0.84 ± 0.02	2.17 ± 0.03	0.39 ± 0.02
NC430	170.10	7240	729.2	0.9991	0.25 ± 0.005	0.79 ± 0.02	1.69 ± 0.07	0.47 ± 0.04
NC427	168.30	7060	731.4	0.6946	0.16 ± 0.003	0.74 ± 0.02	1.97 ± 0.02	0.37 ± 0.02
NC426	167.20	6950	732.8	1.0007	0.19 ± 0.005	0.60 ± 0.02	2.56 ± 0.03	0.23 ± 0.01
NC424	165.10	6740	735.4	1.0031	0.21 ± 0.004	0.65 ± 0.01	2.64 ± 0.01	0.25 ± 0.01
NC421	162.60	6490	738.5	0.9999	0.30 ± 0.006	0.92 ± 0.02	2.09 ± 0.02	0.44 ± 0.02
NC419'	160.60	6290	741.0	1.0036	0.24 ± 0.012	0.75 ± 0.04	2.04 ± 0.09	0.37 ± 0.05
NC419	160.60	6290	741.0	1.0036	0.24 ± 0.007	0.75 ± 0.02	2.04 ± 0.09	0.37 ± 0.04
NC418	159.60	6190	742.3	1.0015	0.32 ± 0.006	0.97 ± 0.02	2.03 ± 0.06	0.48 ± 0.03
NC417	158.30	6060	743.9	0.9159	0.24 ± 0.005	0.81 ± 0.02	2.33 ± 0.02	0.35 ± 0.02
NC416	157.30	5960	745.2	1.0010	0.20 ± 0.004	0.62 ± 0.01	3.19 ± 0.01	0.19 ± 0.01
NC415	156.30	5860	746.4	0.9993	0.28 ± 0.005	0.86 ± 0.01	2.81 ± 0.02	0.31 ± 0.01
NC413	154.60	5690	748.5	0.5365	0.12 ± 0.003	0.67 ± 0.01	2.74 ± 0.06	0.25 ± 0.01
NC411	152.60	5490	751.0	1.0004	0.23 ± 0.004	0.72 ± 0.01	3.22 ± 0.03	0.22 ± 0.01
NC409	151.10	5340	752.9	1.0033	0.31 ± 0.005	0.96 ± 0.02	2.72 ± 0.03	0.35 ± 0.02
NC408	150.40	5270	753.8	1.0008	0.30 ± 0.005	0.93 ± 0.02	2.67 ± 0.04	0.35 ± 0.02
NC407	148.90	5120	755.7	1.0013	0.30 ± 0.005	0.93 ± 0.02	2.90 ± 0.05	0.32 ± 0.02
NC404	146.40	4870	758.8	1.0005	0.24 ± 0.005	0.75 ± 0.01	2.23 ± 0.02	0.34 ± 0.01
NCJ34	145.80	4810	759.5	0.9997	0.10 ± 0.003	0.31 ± 0.01	2.46 ± 0.05	0.12 ± 0.01
NC403	145.60	4790	759.8	1.0032	0.30 ± 0.005	0.90 ± 0.01	2.80 ± 0.07	0.32 ± 0.02
NC402	141.40	4370	765.0	1.0010	0.31 ± 0.007	0.97 ± 0.02	2.78 ± 0.03	0.35 ± 0.02
NC401	140.95	4325	765.6	1.0025	0.32 ± 0.005	1.01 ± 0.02	3.22 ± 0.04	0.31 ± 0.01
NC400	140.20	4250	766.5	0.5175	0.12 ± 0.003	0.73 ± 0.02	2.58 ± 0.05	0.28 ± 0.02
NC322	139.10	4140	767.9	1.0013	0.19 ± 0.004	0.61 ± 0.01	3.45 ± 0.05	0.18 ± 0.01
NC320	138.50	4080	768.7	1.0012	0.34 ± 0.006	1.06 ± 0.02	2.46 ± 0.05	0.43 ± 0.02
NC319	138.25	4055	769.0	1.0013	0.32 ± 0.006	1.00 ± 0.02	2.77 ± 0.03	0.36 ± 0.01
NC317	137.80	4010	769.5	1.0015	0.31 ± 0.006	0.97 ± 0.02	3.01 ± 0.08	0.32 ± 0.02
NC316	137.50	3980	769.9	1.0020	0.33 ± 0.006	1.03 ± 0.02	3.45 ± 0.06	0.30 ± 0.01
NC315	137.20	3950	770.3	1.0017	0.42 ± 0.009	1.32 ± 0.03	2.76 ± 0.02	0.48 ± 0.02
NC314	137.00	3930	770.5	0.9998	0.43 ± 0.007	1.36 ± 0.02	2.70 ± 0.08	0.50 ± 0.03
NC313	136.70	3900	770.9	1.0009	0.40 ± 0.007	1.25 ± 0.02	2.80 ± 0.02	0.45 ± 0.02
NC312	136.40	3870	771.3	1.0019	0.42 ± 0.007	1.30 ± 0.02	3.01 ± 0.08	0.43 ± 0.03
NC311	136.05	3835	771.7	1.0014	0.41 ± 0.008	1.29 ± 0.03	2.70 ± 0.04	0.48 ± 0.02
NC310	135.65	3795	772.2	1.0010	0.41 ± 0.008	1.28 ± 0.02	3.39 ± 0.07	0.38 ± 0.02
NC309	135.45	3775	772.5	1.0020	0.34 ± 0.009	1.08 ± 0.03	2.94 ± 0.06	0.37 ± 0.02
NC308	135.20	3750	772.8	1.0035	0.44 ± 0.007	1.39 ± 0.02	2.68 ± 0.04	0.52 ± 0.02
NC307	135.00	3730	773.0	1.0017	0.34 ± 0.007	1.08 ± 0.02	2.92 ± 0.06	0.37 ± 0.02
MJ-XXII-4	134.85	3715	773.2	1.0014	0.30 ± 0.006	0.95 ± 0.02	3.08 ± 0.02	0.31 ± 0.01
MJ-XXII-3	134.67	3697	773.4	1.0005	0.21 ± 0.006	0.66 ± 0.02	3.72 ± 0.07	0.18 ± 0.01
NC306	134.55	3685	773.6	1.0013	0.22 ± 0.005	0.69 ± 0.01	3.34 ± 0.06	0.21 ± 0.01
MJ-XXII-2	134.48	3678	773.7	0.9994	0.11 ± 0.004	0.34 ± 0.01	7.97 ± 0.19	0.04 ± 0.00
MJ-XXII-2'	134.48	3678	773.7	1.0013	0.11 ± 0.004	0.35 ± 0.01	8.06 ± 0.21	0.04 ± 0.00
MJ-XXII-2"	134.48	3678	773.7	1.0002	0.13 ± 0.003	0.40 ± 0.01	8.44 ± 0.09	0.05 ± 0.00
v4	134.30	3660	773.9	1.0005	0.10 ± 0.002	0.30 ± 0.01	5.28 ± 0.11	0.06 ± 0.00
MJ-XXII-1	134.30	3660	773.9	1.0004	0.19 ± 0.004	0.60 ± 0.01	6.82 ± 0.11	0.09 ± 0.00
MJ-XXII-1'	134.30	3660	773.9	1.0020	0.20 ± 0.004	0.62 ± 0.01	6.61 ± 0.12	0.09 ± 0.00
MJ-XXII-1	134.30	3660	773.9	0.9997	0.23 ± 0.004	0.71 ± 0.01	6.97 ± 0.09	0.10 ± 0.00
MJ-XXI-5	134.29	3659	773.9	1.0007	0.22 ± 0.004	0.70 ± 0.01	5.25 ± 0.04	0.13 ± 0.01
NC304	134.20	3650	774.0	1.0020	0.45 ± 0.008	1.41 ± 0.02	2.48 ± 0.07	0.57 ± 0.04
NC303	133.80	3610	774.5	1.0004	0.47 ± 0.008	1.47 ± 0.03	2.50 ± 0.06	0.59 ± 0.04
NC302	133.50	3580	774.9	1.0010	0.47 ± 0.008	1.47 ± 0.02	2.51 ± 0.07	0.59 ± 0.04
NC301	133.20	3550	775.3	1.0010	0.49 ± 0.008	1.54 ± 0.02	2.63 ± 0.04	0.58 ± 0.03
NC298	132.25	3455	776.5	1.0014	0.35 ± 0.012	1.10 ± 0.04	2.88 ± 0.07	0.38 ± 0.03
NC295	131.45	3375	777.5	1.0013	0.32 ± 0.006	1.00 ± 0.02	2.64 ± 0.05	0.38 ± 0.02
MJ-XIX-4	131.44	3374	777.5	1.0003	0.29 ± 0.011	0.92 ± 0.03	2.66 ± 0.07	0.34 ± 0.03
NC293	131.00	3330	778.0	1.0016	0.34 ± 0.006	1.07 ± 0.02	2.85 ± 0.03	0.37 ± 0.01
MJ-XIX-1	130.89	3319	778.2	1.0000	0.33 ± 0.008	1.05 ± 0.02	3.00 ± 0.08	0.35 ± 0.02
MJ-XVIII-7	130.70	3300	778.4	1.0010	0.31 ± 0.006	0.97 ± 0.02	2.63 ± 0.06	0.37 ± 0.02
MJ-XVIII-6	130.51	3281	778.6	1.0005	0.30 ± 0.006	0.96 ± 0.02	2.76 ± 0.05	0.35 ± 0.02
NC290	130.30	3260	778.9	1.0023	0.33 ± 0.006	1.04 ± 0.02	2.76 ± 0.08	0.38 ± 0.03
NC289	130.15	3245	779.1	1.0016	0.26 ± 0.005	0.81 ± 0.02	3.18 ± 0.03	0.26 ± 0.01
NC285	129.45	3175	780.0	1.0033	0.27 ± 0.005	0.84 ± 0.01	2.79 ± 0.08	0.30 ± 0.02
NC280	128.30	3060	781.4	1.0006	0.20 ± 0.008	0.61 ± 0.03	2.55 ± 0.02	0.24 ± 0.02
NC280'	128.30	3060	781.4	1.0006	0.20 ± 0.006	0.62 ± 0.02	2.55 ± 0.02	0.24 ± 0.02
NC278	128.20	3050	781.5	1.0024	0.26 ± 0.006	0.83 ± 0.02	2.51 ± 0.03	0.33 ± 0.02
NC276	127.90	3020	781.9	1.0019	0.21 ± 0.004	0.67 ± 0.01	2.14 ± 0.04	0.31 ± 0.02
NC274	127.60	2990	782.3	0.9997	0.24 ± 0.004	0.76 ± 0.01	2.27 ± 0.05	0.34 ± 0.02
NC273	127.30	2960	782.7	0.9999	0.22 ± 0.004	0.70 ± 0.01	2.31 ± 0.03	0.30 ± 0.01
NC271	127.00	2930	783.0	0.9993	0.16 ± 0.003	0.49 ± 0.01	3.19 ± 0.08	0.15 ± 0.01
NC265	126.40	2870	783.8	1.0011	0.18 ± 0.004	0.56 ± 0.01	2.42 ± 0.03	0.23 ± 0.01
NC260a	125.50	2780	784.9	1.0008	0.16 ± 0.003	0.49 ± 0.01	2.22 ± 0.02	0.22 ± 0.01
NC258a	125.00	2730	785.41	1.0035	0.08 ± 0.002	0.26 ± 0.01	3.39 ± 0.05	0.08 ± 0.00

(*continued on next page*)

Table 1 (*continued*)

Sample codes	Depth MJS composite (m)	Depth Ideale section (cm)	Age model (ka)	Sample weight [g]	Measured (^{10}Be/^{9}Be) $*10^{-11}$	Authigenic decay corrected ^{10}Be $*10^{8}$ [at·g^{-1}]	Authigenic ^{9}Be $*10^{16}$ [at·g^{-1}]	Authigenic ^{10}Be/^{9}Be $*10^{-8}$
NC257	124.70	2700	785.59	1.0013	0.12 ± 0.003	0.36 ± 0.01	2.73 ± 0.01	0.13 ± 0.01
NC256a	124.40	2670	785.77	1.0011	0.14 ± 0.003	0.44 ± 0.01	2.66 ± 0.05	0.17 ± 0.01
NC253c	123.60	2590	786.24	1.0022	0.14 ± 0.003	0.45 ± 0.01	2.69 ± 0.08	0.17 ± 0.01
NC250c	122.30	2460	787.01	1.0025	0.16 ± 0.003	0.50 ± 0.01	2.21 ± 0.06	0.23 ± 0.02
NC246	121.05	2335	787.74	1.0023	0.17 ± 0.003	0.53 ± 0.01	2.23 ± 0.06	0.24 ± 0.02
NC243	120.15	2245	788.27	0.9996	0.18 ± 0.004	0.56 ± 0.01	2.23 ± 0.02	0.25 ± 0.01
NC239	119.10	2140	788.89	1.0011	0.18 ± 0.003	0.55 ± 0.01	2.35 ± 0.05	0.24 ± 0.01
NC236	118.60	2090	789.19	1.0007	0.20 ± 0.004	0.63 ± 0.01	2.42 ± 0.04	0.26 ± 0.01
NC231	117.70	2000	789.72	1.0002	0.18 ± 0.004	0.56 ± 0.01	2.37 ± 0.05	0.24 ± 0.01
NC228	117.30	1960	789.96	0.9997	0.19 ± 0.004	0.60 ± 0.01	2.60 ± 0.04	0.23 ± 0.01
NC226	116.90	1920	790.19	0.9987	0.19 ± 0.003	0.58 ± 0.01	2.89 ± 0.06	0.20 ± 0.01
NC225	116.60	1890	790.37	1.0030	0.21 ± 0.004	0.64 ± 0.01	2.43 ± 0.06	0.27 ± 0.02
NC219	115.80	1810	790.84	1.0017	0.19 ± 0.004	0.60 ± 0.01	2.81 ± 0.03	0.21 ± 0.01
NC217s	115.25	1755	791.17	1.0017	0.18 ± 0.004	0.57 ± 0.01	2.37 ± 0.06	0.24 ± 0.02
NC215	115.00	1730	791.31	1.0007	0.17 ± 0.003	0.53 ± 0.01	2.29 ± 0.01	0.23 ± 0.01
NC208	113.95	1625	791.93	0.9998	0.20 ± 0.004	0.63 ± 0.01	2.42 ± 0.06	0.26 ± 0.02
NC206	113.70	1600	792.08	1.0010	0.20 ± 0.004	0.63 ± 0.01	2.53 ± 0.02	0.25 ± 0.01
NC201s	112.85	1515	792.58	0.9992	0.24 ± 0.004	0.75 ± 0.01	2.74 ± 0.04	0.27 ± 0.01
NC199	112.60	1490	792.73	1.0010	0.21 ± 0.004	0.65 ± 0.01	2.37 ± 0.06	0.27 ± 0.02
NC191	110.90	1320	793.73	0.9997	0.21 ± 0.004	0.68 ± 0.01	2.33 ± 0.02	0.29 ± 0.01
NC186	109.40	1170	794.62	1.0016	0.19 ± 0.004	0.59 ± 0.01	2.31 ± 0.04	0.25 ± 0.01
NC179	107.90	1020	795.50	1.0004	0.23 ± 0.004	0.71 ± 0.01	2.31 ± 0.04	0.31 ± 0.01
NC174	106.80	910	796.15	1.0013	0.21 ± 0.004	0.65 ± 0.01	2.59 ± 0.05	0.25 ± 0.01
v3	105.80	820	796.68	1.0017	0.09 ± 0.002	0.29 ± 0.01	8.39 ± 0.05	0.03 ± 0.00
MJE-4	105.70	810	796.74	1.0003	0.14 ± 0.003	0.43 ± 0.01	4.39 ± 0.06	0.10 ± 0.01
NC168	105.10	750	797.10	1.0007	0.25 ± 0.005	0.77 ± 0.01	2.24 ± 0.05	0.34 ± 0.02
NC161	103.90	630	797.80	1.0001	0.20 ± 0.004	0.64 ± 0.01	2.20 ± 0.03	0.29 ± 0.01
NC150	101.45	385	799.25	1.0006	0.18 ± 0.003	0.58 ± 0.01	2.43 ± 0.03	0.24 ± 0.01
NC145	100.40	280	799.87	1.0000	0.18 ± 0.003	0.56 ± 0.01	2.05 ± 0.03	0.27 ± 0.01
DFJ74	97.60	0	801.52	1.0015	0.17 ± 0.004	0.55 ± 0.01	2.20 ± 0.05	0.25 ± 0.02
	Mean ± std. Dev.				0.24 ± 0.10	0.77 ± 0.30	3.03 ± 1.37	0.29 ± 0.13

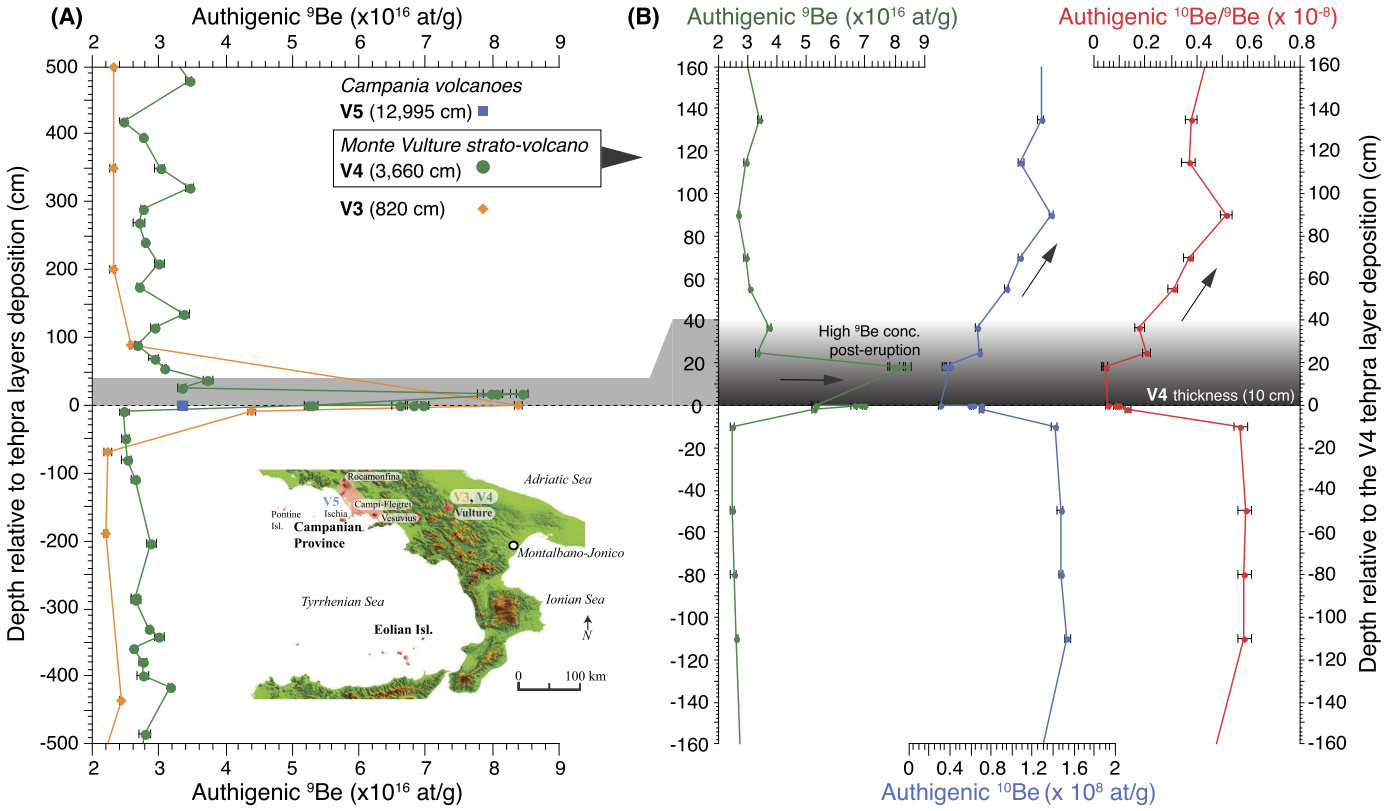

Fig. 3. Authigenic Be isotope signature within the tephra layers. Results are presented on depth relative to tephra layers. Negative (positive) values are for the depth before (after) the tephra layer deposition. (A) Authigenic ^{9}Be concentration of V3–V4–V5 tephra layers. The ^{9}Be signature for V3 (orange diamonds) and V4 (green circle) presents similar spikes, while ^{9}Be concentration for the V5 sample (blue square) is significantly lower. (B) Results of ^{10}Be (blue), ^{9}Be (green) and ^{10}Be/^{9}Be ratio (red) above and below the V4 tephra layer. The total depth interval represents a 3 ka duration period. High ^{9}Be concentrations coeval with sharp ^{10}Be and ^{10}Be/^{9}Be ratio decreases are found within, and immediately above, the tephra layer precluding any geomagnetic interpretation of the ^{10}Be/^{9}Be ratio in this specific layer (highlighted by grey bar). (For interpretation of the references to color in this figure legend, the reader is referred to the web version of this article.)

(Fig. 3B). This specific interval is arguably associated with eruption and post-eruption Be scavenging condition changes and ^{10}Be dilution by the rapid tephra deposition, not directly related with atmospheric ^{10}Be production changes. Moreover, the coarse grain size depicted by relatively high sand percentages in this interval (Fig. 2E) likely results in lower scavenging efficiency of dissolved ^{10}Be (Simon et al., 2016b). Above this interval, the ^{10}Be concentrations vary around an average of $0.84 \pm 0.20 \times 10^8$ at/g (phases 4 and 5) except for one outlier at 4,810 cm that presents a very low value of 0.31×10^8 at/g.

5.3. Authigenic ^{10}Be/^{9}Be ratio

The authigenic ^{10}Be/^{9}Be ratios vary between 0.04 and 0.59×10^{-8} with an average value of $0.29 \pm 0.13 \times 10^{-8}$ (Fig. 2H). Such low average ^{10}Be/^{9}Be ratios ($<1 \times 10^{-8}$) correspond to typical values for environments experiencing high terrigenous inputs (e.g. Brown et al., 1992; Simon et al., 2016b). The ^{10}Be/^{9}Be ratio curve mimics the ^{10}Be variation mainly characterized by a major enhancement interval (phase 3). Within phase 1, the ^{10}Be/^{9}Be ratio has a mean value of $0.24 \pm 0.05 \times 10^{-8}$ and smoothly decrease to 0.08×10^{-8}. This period is followed by a rather constant increases of the ^{10}Be/^{9}Be ratio (phase 2) that stabilized to a plateau at $0.37 \pm 0.01 \times 10^{-8}$ within the 3,260–3,455 cm interval. The highest ^{10}Be/^{9}Be ratios corresponding to maximal values of the Ideale section peak at $0.58 \pm 0.01 \times 10^{-8}$ within the 3,550–3,650 cm interval (Fig. 2H). This represents a near doubling of the ^{10}Be/^{9}Be ratio compared to the preceding interval (0.26×10^{-8} from 0 to 3,455 cm). That sequence is followed by a sharp drop of the ^{10}Be/^{9}Be ratios ($0.20 \pm 0.16 \times 10^{-8}$) associated with sediments deposited during and immediately after the V4 event (Figs. 2H and 3B). This near collapse of the ^{10}Be/^{9}Be ratio within this short interval coincides with harsh geochemical condition changes associated with the tephra layer deposition (see above). The interval from 3,750 to 3,950 cm comprises high ^{10}Be/^{9}Be ratios with mean value of $0.45 \pm 0.06 \times 10^{-8}$. Altogether, when removing the layer disturbed by the tephra signal, the highest ^{10}Be/^{9}Be ratio values from the Ideale section, i.e. $0.50 \pm 0.08 \times 10^{-8}$, are found in two distinct stages between 3,550 and 3,950 cm (phase 3). From 3,980 to 6,060 cm, phase 4, the authigenic ^{10}Be/^{9}Be ratios return to average mean $0.30 \pm 0.07 \times 10^{-8}$, slightly higher than those recorded before the major enhancement of phase 3. The ^{10}Be/^{9}Be ratios experienced some fluctuation and two sharp lows at 4,140 and 4,810 cm depth. Phase 5 starting at 6,060 cm is characterized by two ^{10}Be/^{9}Be ratio increases (Fig. 2H). These peaks are not present in the ^{10}Be signal but clearly correspond to two significant ^{9}Be-lows (Fig. 2F) associated with period of enhanced erosional processes on carbonate (dolomitic) and arenitic bedrock units, coarser grain size fraction supply (Fig. 2E) and coccolith reworking during cold periods (Maiorano et al., 2016). A clearer picture of those environmental changes at the end of MIS 19a to MIS 18 transition is requested in order to settle this conundrum and to propose robust geomagnetic interpretation of the ^{10}Be/^{9}Be ratios (Fig. 2H). Except for this specific interval, the absence of correlation with environmental proxies or sea level changes (Fig. 2 and Table S2) supports geomagnetic interpretation of the authigenic ^{10}Be/^{9}Be ratio fluctuations in the Ideale section.

5.4. Stable isotopic stratigraphy

The *Melonis barleanum* δ^{18}O data vary between ~0.6 and 2.6‰ (Fig. 2A). They provide a marine isotopic record of the T.IX and of the MIS 19 structure at an unprecedented average time-resolution of ~120–250 years (see section 6). The deglaciation is 16 m-thick, taking place between 1,240 and 2,860 cm. It corresponds to a decrease of nearly 2‰ of the δ^{18}O values, which range from ~2.6‰, at the glacial maximum, to ~0.6‰ at the peak of MIS 19c. It is noteworthy that the deglaciation is characterized by a clear return to more glacial conditions between 1,900 and 2,200 cm, a structure that closely resembles the Younger Dryas episode of Termination I (T.I; Fig. 2A). Paleotemperature reconstructions are mandatory to disentangle the benthic δ^{18}O signal and decipher whether this return to more glacial values was chiefly due to a drop in marine temperature as suggested by planktonic foraminifera assemblage (Fig. 2B), or an increase in seawater δ^{18}O.

From the peak value of MIS 19c, at ~2,860 cm, the benthic δ^{18}O record shows a rather progressive increase upward with minor scale oscillations until about 3,960 cm, where it reaches ~1.8‰. Then, the δ^{18}O record shows an extremely abrupt decrease, with values dropping by more than 0.7‰ (from 1.83 to 1.10‰) in only 40 cm, and by ~1‰ in one meter (Fig. 2A). This abrupt shift marks the beginning of the upper interval of our sampled section, which is characterized by relatively stable intervals with low δ^{18}O values (suggesting a return to interglacial conditions), limited by extremely abrupt δ^{18}O changes at their onsets and terminations. Two such episodes are clearly visible in our δ^{18}O record (over the intervals 3,994–4,987 cm, and 5,500–6,110 cm, respectively). The abrupt δ^{18}O decrease at the upper end of the sampled interval suggests that a third episode may exist above it, a hypothesis that will be tested in the future by extending the high-resolution record upward.

At the abrupt onsets and ends of these warm intervals, our data suggest that seawater δ^{18}O may have changed by up to 0.5‰ or temperature may have changed by up to 2 °C over no less than 250 years (see discussion about age model, below). Those changes were likely connected to the abrupt oscillations observed in the isotopic record of the Sulmona paleolake (Central Italy), which were attributed to changes in the lake hydrological budget (Giacco et al., 2015). Those oscillations resemble the rapid oscillations observed in the δ^{18}O record from MIS 19a in the North Atlantic (Channell et al., 2010; Ferretti et al., 2015; Sánchez Goñi et al., 2016) or in the δD and CH_4 records from EPICA Dome C (Pol et al., 2010). Significant correlations of our new δ^{18}O record with micropaleontological proxies, mineralogy, grain size and relative sea level variations (Fig. 2; Table S2) (see Maiorano et al., 2016 for details), clearly concur with the occurrence of large climate cycles during the MIS 19a (see section 3). The exact paleoclimatic implication of the new Montalbano record is out of the scope of the present work and will be addressed in a dedicated paper in preparation.

6. Chronological framework for the Montalbano Jonico MIS 19 sequence

The chronological framework of the Ideale section discussed in previous studies is mainly based on two ^{40}Ar/^{39}Ar ages (Petrosino et al., 2015) together with a slight tuning of the low-resolution benthic δ^{18}O record (Fig. 1; Marino et al., 2015) to the LR04 benthic stack of Lisiecki and Raymo (2005). However, the large V3 analytical uncertainty (i.e. ±19.5 ka) clearly questions the relevance of using the V3 age as an accurate tie point to establish a precise chronological framework. Moreover, the tuning of benthic δ^{18}O record with global stack such as the LR04 neglects regional differences of several thousand years during glacial terminations (Lisiecki and Stern, 2016) potentially generating large deviations. In this study, we propose an original chronological template using a mix astronomical and radiometric approach in order to overcome these limitations.

We have first created a δ^{18}O stack based on two high-resolution MIS 1/T.I records recovered close to the Montalbano sequence (Fig. 1), i.e. MD90-917 (Siani et al., 2004) and MD90-918 (Caron et al., 2012), and for which age models are based on radiocar-

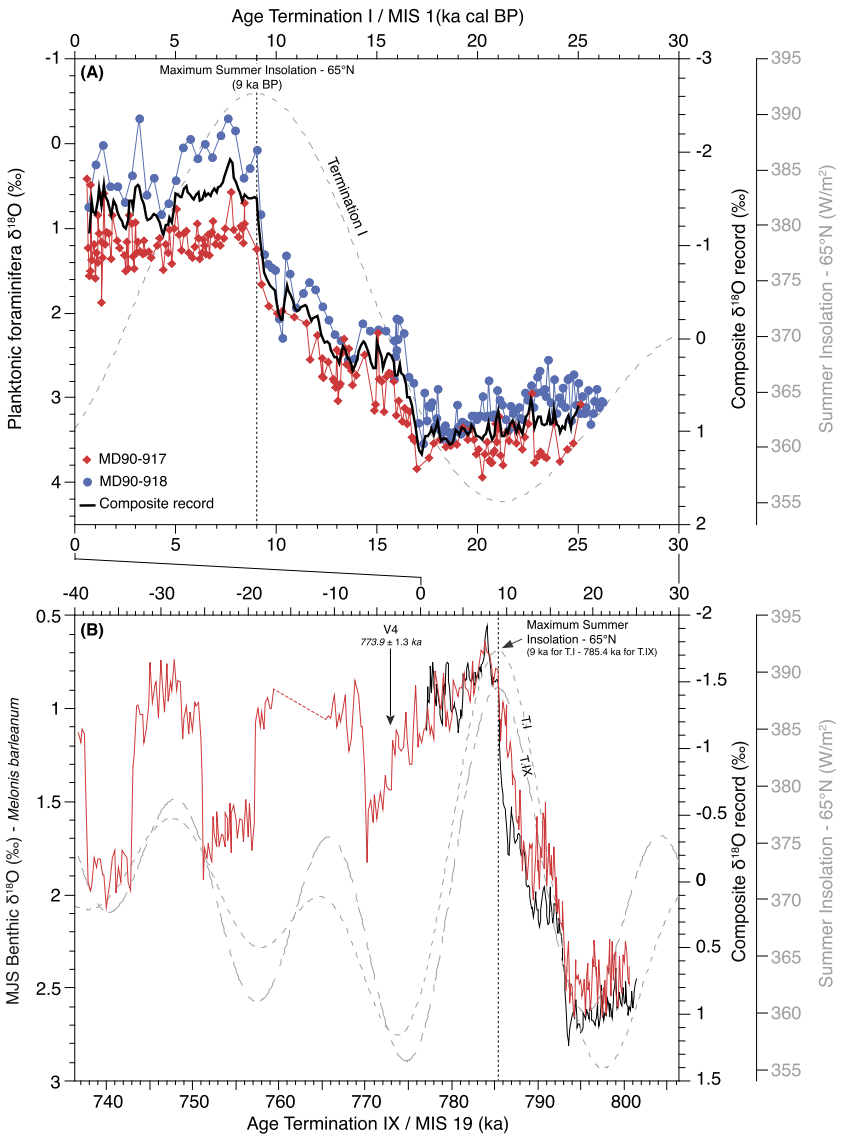

Fig. 4. Chronological framework of the Ideale section. (A) Termination I/MIS 1 planktonic δ^{18}O stack from nearby marine cores (MD90-917 and MD90-918, see text for details). (B) High-resolution benthic δ^{18}O record of Termination IX (T.IX) from the Ideale section (red curve) fine-tuned to the Termination I (T.I) planktonic δ^{18}O stack (black curve), assuming similar orbital forcing and CO_2 levels between T.I and T.IX (see text), and adjusted using the V4 radiometric date (Petrosino et al., 2015). Summer insolation (JAS) is from Laskar et al. (2004). (For interpretation of the references to color in this figure legend, the reader is referred to the web version of this article.)

bon dates. This regional stack confirmed that the summer insolation maximum (65°N; Laskar et al., 2004; i.e. 9 ka) is in phase with the deglaciation (Fig. 4A). Then, we used the similarity of orbital forcing (i.e. precession minimum and obliquity maximum in phase, low eccentricity) and CO_2 levels between the two MIS 1 and MIS 19c periods (Pol et al., 2010; Tzedakis et al., 2012; Giacco et al., 2015; Bereiter et al., 2015; Ferretti et al., 2015; Yin and Berger, 2015) as benchmark to limit the hypotheses underlying the astrochronological approach (leads and lags with the orbital forcing). We assume that similar phase relationships exist between the summer insolation curve (65°N) and the δ^{18}O response to adjust T.IX with T.I. We used the peak of maximum isolation (i.e. 785.4 ka) associated with the T.IX that is equivalent to 9 ka for T.I (Fig. 4B) to synchronize both terminations. The best fit between T.IX and T.I in term of structure and duration is thus achieved using a mean sedimentation rate of 170 cm/ka (Fig. 4B). We extrapolated downward this sedimentation rate to establish the late MIS 20 chronology. This method gives a V3 age of 796.6 ka, which is 4.6 ka younger than the ^{40}Ar/^{39}Ar age of Petrosino et al. (2015), but well within its uncertainty (Table S3).

Following the onset of MIS 19c, the chronology is settled by linear interpolation using the age of V4 at 773.9 ka (Petrosino et al., 2015). This choice is justified by all recent ^{40}Ar/^{39}Ar calibration results pointing toward ACs ages close to 1.185 Ma (Jicha et al., 2016; Niespolo et al., 2016) that endorses the robustness of the V4 age of Petrosino et al. (2015) (Table S3). The derived sedimentation rate (i.e. 80 cm/ka) is then extrapolated onward (Fig. 2C) to set up the MIS 19a chronology (Fig. 4B). This chronological framework places the red interval identified in the MJS as a "ghost sapropel" (Maiorano et al., 2016) at 784 ka, synchronous with the i-cycle 74 from the Ionian Sea core KC01b (Lourens, 2004). It yields a MIS 19c duration of ~11.2 ka, in agreement with the duration of MIS 19c recorded in the lacustrine Sulmona section (i.e. 10.8 ka; Giaccio et al., 2015) or implied by North Atlantic records (i.e. 10.5–12.5 ka; Tzedakis et al., 2012). Although we recognize that the extrapolation above V4 is probably an oversimplified solution and that sedimentation rates might have varied correspondingly with the large MIS 19a oscillations (Fig. 2), our new chronology places adequately the two stable MIS 19a "interglacials" characterized by low δ^{18}O values synchronous to summer insolation maxima (Fig. 4B).

The completion of the ongoing high-resolution $\delta^{18}O$ record will contribute to propose (or confirm) a more robust chronological framework for the upper part of the Ideale section in the near future. Note that the resolution of our age model is solid within the MBB interval, thanks to the stratigraphical position and age of V4.

7. Discussion

7.1. Identification and chronostratigraphic position of the MBB

Detailed authigenic $^{10}Be/^{9}Be$ ratio results obtained from an averaged 26 cm sample spacing (~325 years) along the MIS 19c–b interval from the Ideale section are described by the succession of several phases based on their distinct signatures. No significant correlations were found between the authigenic $^{10}Be/^{9}Be$ ratio and local sea level variations (Fig. 2C), nor with any of the available high resolution paleoenvironmental proxies (Table S2; Maiorano et al., 2016) during phases 1 to 4 that cover the MIS 20 to MIS 19a interval (Fig. 2), supporting geomagnetic interpretation. This is particularly important since strong environmental imprints can prevail on authigenic Be ratio records from shallow marine shelf environments or semi-enclosed basins, leading to very large ^{10}Be concentration changes (up to 10 times) as previously demonstrated in the Wanganui Basin (New Zealand; Graham et al., 1998) or in Baffin Bay (Simon et al., 2016b). It thus clearly identifies a ^{10}Be overproduction episode associated with low geomagnetic dipole moments (GDM) within phase 3 (Fig. 2I). This ^{10}Be overproduction episode begins during late MIS 19c and extends over the MIS 19b period according to our high-resolution benthic oxygen isotope record (Fig. 5A).

The absolute age of the MBB – defined as the mid-slope of the VGP transition path or the dipole moment low (RPI low) – has been debated since its first reliable astrochronological dating by Shackleton et al. (1990). This MBB age falls into two main age groups centered at: ~772–773 and ~780–781 ka (Table 1 in Head and Gibbard, 2015). Given the uncertainties associated with: i) the astrochronological tuning of marine sequences (±4.0 or 5.0 ka), a direct consequence of uncertainties regarding the phase relationship between insolation and climatic changes (Imbrie and Imbrie, 1980); ii) the signal resolution of the sedimentary records; iii) the detrital magnetization processes, especially in low sedimentation rate cores (Valet et al., 2016); and, iv) the $^{40}Ar/^{39}Ar$ dating methods (see Table S3), these two age groups are obviously not significantly distinct and most likely simply arise from age model uncertainties and/or variable timing of magnetization lock-in. This is notably illustrated by a ~10 ka shift of the MBB age between paleomagnetic and ^{10}Be measurements in core MD97-2143 (Fig. 5B) (Suganuma et al., 2010).

Therefore, in order to propose an original discussion, we first compare the stratigraphic position of the MBB in records covering a large latitudinal and longitudinal range and presenting high resolution oxygen stratigraphies along with paleomagnetic and/or ^{10}Be-proxy (authigenic $^{10}Be/^{9}Be$ ratio and ^{10}Be-flux) measurements. In Fig. 5, these records present nearly identical stratigraphic variability features: i.e., ^{10}Be-proxy increase and large RPI drop, that are contemporaneous to the late MIS 19c and MIS 19b time periods (phase 3). This is also consistent with the high-resolution RPI record (i.e. ~60 cm/ka) from Osaka Bay (Hyodo and Kitaba, 2015). Prior to the MBB interval, the four ^{10}Be-records presented in Fig. 5 yield minimal ^{10}Be-proxy at the MIS 19c onset, while the long-term RPI decrease–^{10}Be production increase associated with phase 2 in the marine records spans the entire MIS 19c period (yellow arrow in Fig. 5). Authigenic $^{10}Be/^{9}Be$ ratio and ^{10}Be-flux present thus similar phases 2 and 3 patterns with increasing ^{10}Be-proxy corresponding to decreasing RPI, and maximum ^{10}Be-proxy coeval with the lowest RPI values (Fig. 5). Phase 4 presents distinct behavior of the ^{10}Be-proxy between records obtained from MJS and EPICA Dome C (EDC) ice core and those obtained from marine cores (MD90-0961 and MD97-2143) with a sharper diminution of the ^{10}Be-proxy in the MJS and EDC records. This difference is most likely related to the different sedimentation rates or resolution of both record types (~80 cm/ka in MJS vs ~5 cm/ka for core MD90-0961 or ~1 cm/ka for core MD97-2143).

The contemporaneity of global distribution of directional variations, often chosen to pinpoint reversals, is questioned by the observed slight chronostratigraphic offsets of directional changes between cores (Fig. 5B–D). This might result from i) not globally synchronous directional reversal features associated with non-dipolar transitional field component (Brown et al., 2007; Valet et al., 2016), or ii) unreliable records of transitional directions in low sedimentation rate sequences (Valet et al., 2016). On the contrary, the GDM drop and/or ^{10}Be overproduction associated with the MBB appear synchronous and coherent during the late MIS 19c–b interval in all records (yellow banding in Fig. 5). This suggests that variations in intensity are more accurate and reliable paleomagnetic correlation markers than directional changes.

One intriguing question arises from the absence of ^{10}Be overproduction episode preceding the main signature of the reversal (Fig. 5A) in contradiction with the frequent reporting of a marked RPI low in marine sediments (Fig. 5) or lava flows interpreted as a precursor of the reversal ~18 ka prior to the MBB (e.g. Valet et al., 2014; Singer, 2014). This also appears in contradiction with the ^{10}Be flux peak signaled in the EDC record (Fig. 5E). Given the high-resolution sampling of the MJS, it is highly unlikely that we missed such a large ^{10}Be peak corresponding to the precursor, unless it coincides with the V3 tephra. The latest hypothesis is hardly likely considering that the 5 cm interval corresponding to the V3 layer (Petrosino et al., 2015) represents less than 100 years, nevertheless it cannot be totally discarded. It must be also noted that no indisputable and significant ^{10}Be signature of the precursor in marine sediments can be put forth so far despite small ^{10}Be flux increases interpreted as a sign of the precursor in cores MD98-2187 (Suganuma et al., 2010) and MD97-2140 (Carcaillet et al., 2003). It is thus puzzling that such a large GDM drop, reaching intensity values as low as the reversal itself in the PISO-1500 stack (Channell et al., 2009) (Fig. 5F), is not associated with a large ^{10}Be overproduction episode in marine records, whereas significant ^{10}Be overproduction episodes are revealed for each and all GDM lows linked with excursions of the Brunhes Chron (Simon et al., 2016a). The absence of significant ^{10}Be expression for the precursor is challenging, both for future cosmogenic nuclide research and for comparison between sedimentary and volcanic paleomagnetic data. Before any conclusions on the physics of the precursor and its ^{10}Be signature can be reached, studies dedicated to this question are required on other sediment series.

7.2. Chronology of the MBB

The large ^{10}Be overproduction episode corresponding to the MBB is dated between 776—768.5 (grey bar in Fig. 6) according to our new chronological framework. These limits are defined by mid-slopes corresponding to the large peak interval that circumscribe phase 3. This ^{10}Be overproduction episode is synchronous with the large ^{10}Be-flux peak from the EDC ice core (Raisbeck et al., 2006) that spans the 777–766 ka interval with an age uncertainty of ±6 ka using the AICC2012 age model (Bazin et al., 2013) (Fig. 6E). It is also consistent with (i) the ^{10}Be overproduction observed along the equatorial authigenic $^{10}Be/^{9}Be$ stack (Fig. 6G; Simon et al., 2016a); (ii) the MBB ages from numerous marine records including five high sedimentation rate North Atlantic marine cores comprised between 775.3 and 770.9 ka (Channell et al., 2010); (iii) the large geomagnetic dipole moment collapse ev-

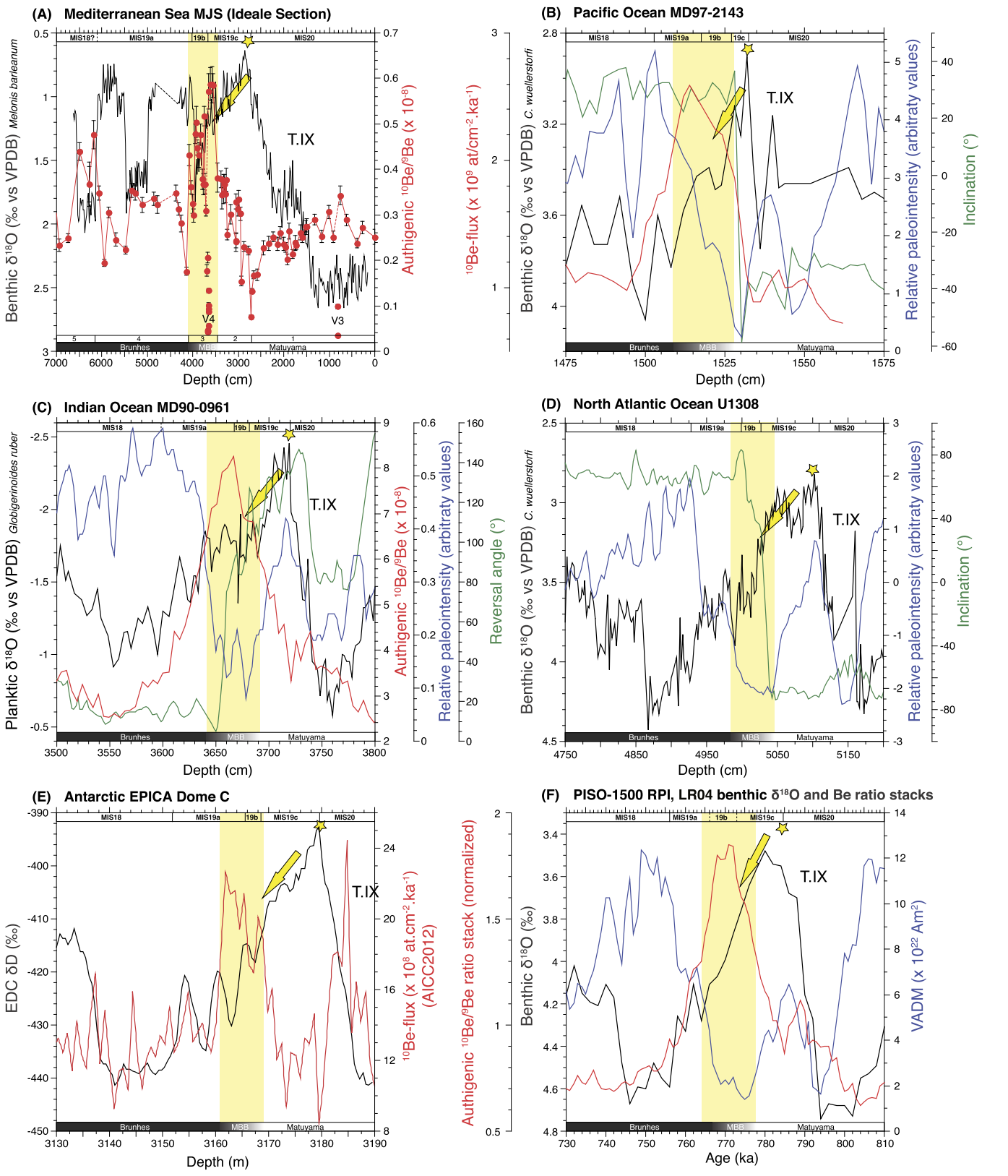

Fig. 5. Climatostratigraphic positioning of the MBB. (A) Authigenic $^{10}Be/^{9}Be$ ratio and benthic $\delta^{18}O$ records from the Ideale section compared to (B) authigenic ^{10}Be-flux (Suganuma et al., 2010), benthic $\delta^{18}O$ record and paleomagnetic results at core MD97-2143 from the Pacific Ocean (Horng et al., 2002); (C) authigenic $^{10}Be/^{9}Be$ ratio, planktic $\delta^{18}O$ record and paleomagnetic results at core MD90-0961 from the Indian Ocean (Valet et al., 2014); (D) benthic $\delta^{18}O$ record and paleomagnetic results at IODP Site U1308 from the North Atlantic Ocean (Channell et al., 2008); (E) δD_{ice} record (Jouzel et al., 2007) and ^{10}Be-flux (Raisbeck et al., 2006) at EPICA Dome C (EDC) from Antarctica; and (F) PISO-1500 RPI stack (Channell et al., 2009), LR04 benthic $\delta^{18}O$ stack (Lisiecki and Raymo, 2005) and equatorial authigenic $^{10}Be/^{9}Be$ ratio stack (Simon et al., 2016a). The yellow stars correspond to the onset of MIS 19c in each series using the lightest $\delta^{18}O$ or lowest δD_{ice} peak. The comparison of these records result in nearly identical climatostratigraphic settings (yellow arrow) of the authigenic $^{10}Be/^{9}Be$ ratio or ^{10}Be-flux enhancement and RPI drop coetaneous to the late MIS 19c – early MIS 19a interval highlighted by the yellow bar. Figure color code: red lines are for ^{10}Be-proxies, black lines are for oxygen isotopes, blue lines are for RPI, green lines represent directional changes. (For interpretation of the references to color in this figure legend, the reader is referred to the web version of this article.)

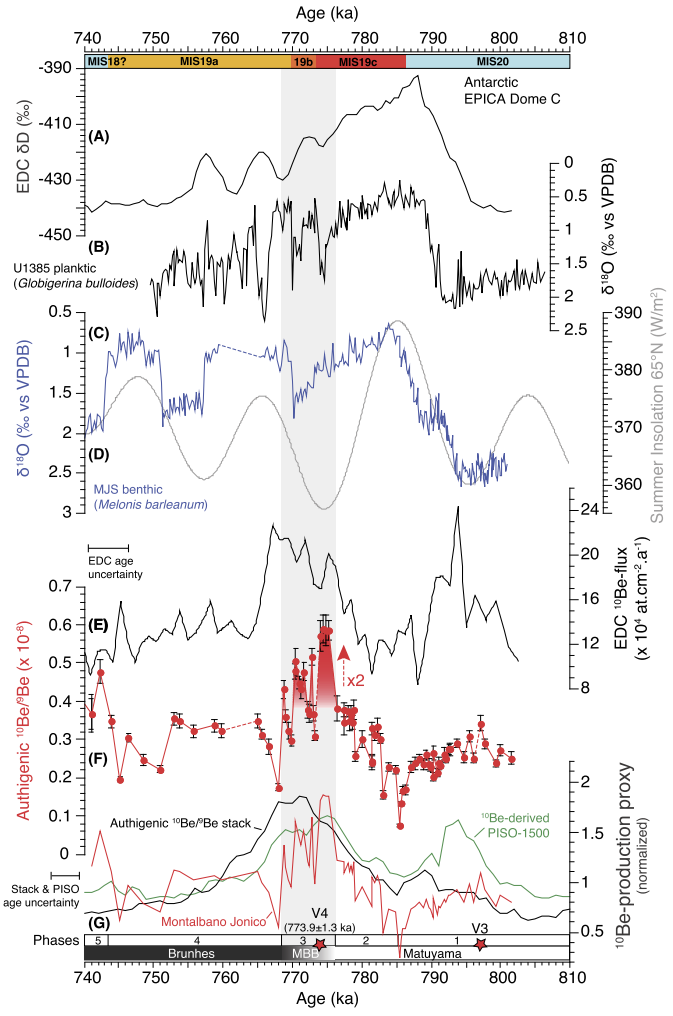

Fig. 6. Chronology of the MBB. Authigenic $^{10}Be/^{9}Be$ ratio (F, red line) and benthic $\delta^{18}O$ *Melonis barleanum* record (C, blue line) from the Ideale section are compared to references. (A) δD_{ice} record and (E) ^{10}Be-fluxes from the Epica Dome C plotted according to the AICC2012 age model (Jouzel et al., 2007; Raisbeck et al., 2006; Bazin et al., 2013). (B) North Atlantic planktic $\delta^{18}O$ record of *Globigerina bulloides* from U1385 (Sánchez Goñi et al., 2016) plotted on the orbital tuned time scale (Hodell et al., 2015). (D) 65°N summer insolation (Laskar et al., 2004). (G) Equatorial authigenic $^{10}Be/^{9}Be$ ratio normalized stack (black; Simon et al., 2016a), authigenic $^{10}Be/^{9}Be$ ratio normalized record from Montalbano Jonico (red) and ^{10}Be-production computed from the PISO-1500 marine sediment RPI stack (green; Channell et al., 2009) using the theoretical ^{10}Be production model of Masarik and Beer (2009). Marine isotopic substages are from this study. The MBB time interval highlighted by grey bar is inferred from the authigenic $^{10}Be/^{9}Be$ ratio peak and geometrically centered at: ~772.5 ka (776–768.5 ka). (For interpretation of the references to color in this figure legend, the reader is referred to the web version of this article.)

idenced in the PISO-1500 stack (Channell et al., 2009) (Figs. 5F and 6G); and, (iv) the MBB age in the Chiba composite section, i.e., 770.2 ± 7.3 ka, estimated from a U–Pb dating of the Byakubi-E tephra at 772.7 ± 7.2 ka (Suganuma et al., 2015). Moreover, the mid-point of the ^{10}Be overproduction peak corresponds to the location of the V4 tephra (Fig. 6) offering the unique opportunity to date radiometrically the mid-point of the MBB interval without any hypothesis on sedimentation rates (e.g. interpolation, gap, mixing).

The largest $^{10}Be/^{9}Be$ ratio peak representing a near doubling of the ^{10}Be production stands from 775.8 to 773.9 ka (Fig. 6F). Such an atmospheric ^{10}Be production doubling is typical of dipole moment collapses associated with reversals (Raisbeck et al., 2006; Valet et al., 2014) or with some of the largest geomagnetic excursions recorded in marine sediments (Ménabréaz et al., 2012, 2014; Horiuchi et al., 2016; Simon et al., 2016a). This ~2 ka period occurring at the end of MIS 19c (Fig. 6C) is associated with the first phase of the GDM collapse characterizing the MBB. The estimated age for this phase is consistent with the $^{40}Ar/^{39}Ar$ date of 776.0 ± 2.0 ka for the transitionally magnetized lava flows from Hawaii and the Canary Islands (Singer et al., 2005). A second and third phases of high ^{10}Be production representing nearly 75% of the maximum peak are observed between 773.0 to 770.2 ka and 769.0 to 768.5 ka, respectively. They likely represent (sub)millennial ^{10}Be production variations (Fig. 6F). Such GDM change rates have been already observed in the best palaeomagnetic records available from globally distributed lava flows (Valet et al., 2012). Decadal to centennial scale duration changes characterizing the MBB interval were also suggested from palaeomagnetic analysis of marine sediments in Japan (Hyodo et al., 2006) and lacustrine sediments in Italy (Sagnotti et al., 2015), together with geomagnetic field numerical model (Brown et al., 2007).

Altogether, the duration of the significant ^{10}Be overproduction episode, i.e., ~7.5 ka, associated with the MBB is within the range of the polarity transition duration given by virtual geomagnetic polar latitude swings or RPI low from marine sedimentary records (e.g. Channell et al., 2009, 2010), or by the ^{10}Be-flux increase at EDC (Raisbeck et al., 2006).

Since atmospheric cosmogenic ^{10}Be production rates are modulated at global scale by the geomagnetic dipole moment, we used theoretical arguments (e.g. Masarik and Beer, 2009) to compute a relative ^{10}Be-production curve from the PISO-1500 calibrated VADM record (Channell et al., 2009). This curve compares favorably with the equatorial authigenic $^{10}Be/^{9}Be$ stack proposed by Simon et al. (2016a) except for the absence of the precursor (see above) (Fig. 6G). The MBB atmospheric ^{10}Be production change retrieved from these two references corresponds to the twofold increase of our authigenic $^{10}Be/^{9}Be$ ratio (Fig. 6F–G), except for the sharper variations observed in the Ideale section (Fig. 6F–G). These variations are most likely resulting from a pronounced smoothing of the authigenic $^{10}Be/^{9}Be$ ratio or RPI signals in "low sedimentation rate" marine cores, hampering the recording of such rapid features in these records.

The GDM dynamics presented in this study through ^{10}Be production changes demonstrate several sharp features rather than smooth collapse and recovery phases associated with the MBB. These signatures, including some very steep changes spanning only few centuries, might either correspond to recording artifact, or alternatively be associated with non-linear processes triggering field reversals (from dipole or non-dipole field components). This outcome is particularly important as it places new constraints for numerical models of the geodynamo with unprecedented time resolution for a marine archive. Additional measurements from the Montalbano Jonico Ideale section will further increase this temporal resolution, providing more confidence in computed GDM variation rates.

8. Conclusion

We provide original authigenic $^{10}Be/^{9}Be$ ratio results and new high-resolution benthic (*Melonis barleanum*) oxygen isotope record from the Ideale section of the Montalbano Jonico Succession (MJS, South Italy) covering Termination IX and MIS 19. A precise $^{40}Ar/^{39}Ar$ date on a tephra layer (V4) is used in addition with the new oxygen isotope stratigraphy to establish a robust chronological framework using the analogy (orbital forcing and CO_2 level) between MIS 1 and MIS 19c. The authigenic $^{10}Be/^{9}Be$ ratio (proxy of atmospheric ^{10}Be production) results yield a reliable signature of the geomagnetic dipole moment collapses that characterized the Matuyama–Brunhes polarity reversal. The twofold increase of the ^{10}Be production is similar to the one described in both marine and ice core records. This episode located within the late MIS 19c and

MIS 19b, is precisely dated between ~776.0 and 768.5 ka, with a duration of 7.5 ka. It is thus synchronous with the large ^{10}Be-flux peak recorded in the EDC ice core, and has the same age as the Matuyama–Brunhes polarity reversal recorded in numerous marine sequences.

The very high-resolution of the Ideale section provided by accumulation rate of 80 cm/ka within MIS 19 allows discussing the structure and assess the chronology of (sub)millennial ^{10}Be-production changes, and thus geomagnetic dipole moment variations, with an unprecedented accuracy in marine archives. Moreover, the V4 tephra layer lying within the MBB interval permits a straightforward radiometric dating of the last reversal. Along with thoughtful stratigraphic and paleoenvironmental investigations, these criteria confirm that the Ideale section is highly appropriate to host the Global Stratotype Section and Point of the Middle Pleistocene.

Acknowledgements

Special thanks are due the LN2C team from CEREGE. The authors particularly want to acknowledge the editor, Martin Frank, and three anonymous reviewers for very constructive and helpful comments that contributed to significantly improve this paper. We also want to acknowledge Jean-Pierre Valet for fruitful discussions. The ASTER AMS national facility (CEREGE, Aix en Provence) is supported by the INSU/CNRS, the IRD and by the ANR through the program "EQUIPEX Investissement d'Avenir". This study is supported by: the ERC advanced grant GA 339899-EDIFICE under the ERC's 7th Framework Program (FP7-IDEA-ERC); Fondi di Ateneo 2014 (University of Bari Aldo Moro – Italy) assigned to M. Marino and by the INSU LEFE 2014 "INTERMED" project assigned to S. Nomade. The research benefited of instrumental upgrades from "Potenziamento Strutturale PONa3_00369 dell'Università degli Studi di Bari, Laboratorio per lo Sviluppo Integrato delle Scienze e delle TEcnologie dei Materiali Avanzati e per dispositivi innovativi (SISTEMA)". This is LSCE contribution 6002.

Appendix A. Supplementary material

Supplementary material related to this article can be found online at http://dx.doi.org/10.1016/j.epsl.2016.11.052.

References

Aiello, G., Barra, D., Parisi, R., 2015. Lower–Middle Pleistocene ostracod assemblages from the Montalbano Jonico section (Basilicata, southern Italy). Quat. Int. 383, 47–73.

Bazin, L., Landais, A., Lemieux-Dudon, B., Toyé Mahamadou Kele, H., Veres, D., Parrenin, F., Martinerie, P., Ritz, C., Capron, E., Lipenkov, V., Loutre, M.-F., Raynaud, D., Vinther, B., Svensson, A., Rasmussen, S.O., Severi, M., Blunier, T., Leuenberger, M., Fischer, H., Masson-Delmotte, V., Chappellaz, J., Wolff, E., 2013. An optimized multi-proxy, multi-site Antarctic ice and gas or- bital chronology (AICC2012): 120–800 ka. Clim. Past 9, 1715–1731. http://dx.doi.org/10.5194/cp-9-1715-2013.

Bereiter, B., Eggleston, S., Schmitt, J., Nehrbass-Ahles, C., Stocker, T.F., Fischer, H., Kipfstuhl, S., Chappellaz, J., 2015. Revision of the EPICA Dome C CO_2 record from 800 to 600 kyr before present. Geophys. Res. Lett. 42, 542–549. http://dx.doi.org/10.1002/2014GL061957.

Bertini, A., Toti, F., Marino, M., Ciaranfi, N., 2015. Vegetation and climate across the Early–Middle Pleistocene transition at the Montalbano Jonico section (southern Italy). Quat. Int. 383, 74–88.

Bourlès, D.L., Raisbeck, G.M., Yiou, F., 1989. ^{10}Be and ^{9}Be in Marine sediments and their potential for dating. Geochim. Cosmochim. Acta 53 (2), 443–452.

Braucher, R., Guillou, V., Bourlès, D.L., Arnold, M., Aumaître, G., Keddadouche, K., Nottoli, E., 2015. Preparation of ASTER in-house ^{10}Be/^{9}Be standard solutions. Nucl. Instrum. Methods Phys. Res., Sect. B, Beam Interact. Mater. Atoms 361, 335–340. http://dx.doi.org/10.1016/j.nimb.2015.06.012.

Brown, E.T., Measures, C.I., Edmond, J.M., Bourlès, D.L., Raisbeck, G.M., Yiou, F., 1992. Continental inputs of beryllium to the oceans. Earth Planet. Sci. Lett. 114 (1), 101–111.

Brown, M.C., Holme, R., Bargery, A., 2007. Exploring the influence of the non-dipole field on magnetic records for field reversals and excursions. Geophys. J. Int. 168, 541–550. http://dx.doi.org/10.1111/j.1365-246X.2006.03234.x.

Carcaillet, J.T., Thouveny, N., Bourlès, D.L., 2003. Geomagnetic moment instability between 0.6 and 1.3 Ma from cosmonuclide evidence. Geophys. Res. Lett. 30 (15), 1792. http://dx.doi.org/10.1029/2003GL017550.

Caron, B., Siani, G., Sulpizio, R., Zanchetta, G., Paterne, M., Santacroce, R., Terna, E., Zanella, E., 2012. Late Pleistocene to Holocene tephrostratigraphic record from the Northern Ionian Sea. Mar. Geol. 311, 41–51.

Casnedi, R., 1988. La Fossa bradanica: origine, sedimentazione e migrazione. Mem. Soc. Geol. Ital. 41, 439–448.

Casnedi, R., Crescenti, U., Tonna, M., 1982. Evoluzione dell'Avanfossa adriatica meridionale nel Plio–Pleistocene sulla base di dati di sottosuolo. Mem. Soc. Geol. Ital. 24, 243–260.

Channell, J.E.T., Hodell, D.A., Xuan, C., Mazaud, A., Stoner, J.S., 2008. Age calibrated relative paleointensity for the last 1.5 Myr at IODP Site U1308 (North Atlantic). Earth Planet. Sci. Lett. 274, 59–71.

Channell, J.E.T., Xuan, C., Hodell, D.A., 2009. Stacking paleointensity and oxygen isotope data for the last 1.5 Myr (PISO-1500). Earth Planet. Sci. Lett. 283 (1–4), 14–23. http://dx.doi.org/10.1016/j.epsl.2009.03.012.

Channell, J.E.T., Hodell, D.A., Singer, B.S., Xuan, C., 2010. Reconciling astrochronological and ^{40}Ar/^{39}Ar ages for the Matuyama–Brunhes boundary in the late Matuyama Chron. Geochem. Geophys. Geosyst. 11, Q0AA12. http://dx.doi.org/10.1029/2010GC003203.

Chmeleff, J., von Blanckenburg, F., Kossert, K., Jakob, D., 2010. Determination of the ^{10}Be half-life by multicollector ICP-MS and liquid scintillation counting. Nucl. Instrum. Methods Phys. Res., Sect. B, Beam Interact. Mater. Atoms 268 (2), 192–199. http://dx.doi.org/10.1016/j.nimb.2009.09.012.

Christl, M., Lippold, J., Steinhilber, F., Bernsdorff, F., Mangini, A., 2010. Reconstruction of global ^{10}Be production over the past 250 ka from highly accumulating Atlantic drift sediments. Quat. Sci. Rev. 29 (19–20), 2663–2672. http://dx.doi.org/10.1016/j.quascirev.2010.06.017.

Ciaranfi, N., Lirer, F., Lirer, L., Lourens, L.J., Maiorano, P., Marino, M., Petrosino, P., Sprovieri, M., Stefanelli, S., Brilli, M., Girone, A., Joannin, S., Pelosi, N., Vallefuoco, M., 2010. Integrated stratigraphy and astronomical tuning of the Lower–Middle Pleistocene Montalbano Jonico land section (southern Italy). Quat. Int. 210, 109–120.

D'Alessandro, A., La Perna, R., Ciaranfi, N., 2003. Response of macrobenthos to changes in paleoenvironment in the Lower–Middle Pleistocene (Lucania Basin, southern Italy). Il Quaternario 16, 167–182.

Ferretti, P., Crowhurst, S.J., Naafs, B.D.A., Barbante, C., 2015. The Marine Isotope Stage 19 in the mid-latitude North Atlantic Ocean: astronomical signature and intra-interglacial variability. Quat. Sci. Rev. 108, 95–110.

Giacco, B., Regattieri, E., Zanchetta, G., Nomade, S., Renne, P.R., Sprain, C.J., Drysdale, R.N., Tzedakis, P.C., Messina, P., Scardia, G., Sposato, A., Bassinot, F., 2015. Duration and dynamics of the best orbital analogue to the present interglacial. Geology 43 (7), 603–606.

Girone, A., Capotondi, L., Ciaranfi, N., Di Leo, P., Lirer, F., Maiorano, P., Marino, M., Pelosi, N., Pulice, I., 2013. Paleoenvironmental change at the Lower Pleistocene Montalbano Jonico section (southern Italy): global versus regional signals. Palaeogeogr. Palaeoclimatol. Palaeoecol. 371, 62–79.

Graham, I.J., Robert, L., Ditchburn, G., Whitehead, N.E., 1998. ^{10}Be spikes in Plio–Pleistocene cyclothems, Wanganui Basin, New Zealand: identification of the local flooding surface (LFS). Sediment. Geol. 122, 193–215.

Head, M.J., Gibbard, P.J., 2015. Early–Middle Pleistocene transitions: linking terrestrial and marine realms. Quat. Int. 383, 4–35.

Hodell, D.A., Lourens, L., Crowhurst, S., Konijnendijk, T., Tjallingii, R., Jiménez-Espejo, F., Skinner, L., Tzedakis, P.C., Shackleton Site Project Members, 2015. A reference time scale for site U1385 (Shackleton Site) on the Iberian Margin. Glob. Planet. Change 133, 49–64.

Horiuchi, K., Kamata, K., Maejima, S., Sasaki, S., Sasaki, N., Yamazaki, T., Fujita, S., Motoyama, H., Matsuzaki, H., 2016. Multiple ^{10}Be records revealing the history of cosmic-ray variations across the Iceland Basin excursion. Earth Planet. Sci. Lett. 440, 105–114.

Horng, C.S., Lee, M.Y., Palike, H., Wei, K.Y., Liang, W.T., Iizuka, Y., Torii, M., 2002. Astronomically calibrated ages for geomagnetic reversals within the Matuyama chron. Earth Planets Space 54, 679–690.

Hyodo, M., Biawas, D.K., Noda, T., Tomioka, N., Mishima, T., Itota, C., Sato, H., 2006. Millennial to submillennial-scale features of the Matuyama–Brunhes geomagnetic polarity transition from Osaka Bay, southwestern Japan. J. Geophys. Res., Solid Earth 111. http://dx.doi.org/10.1029/72004JB3584.

Hyodo, M., Kitaba, I., 2015. Timing of the Matuyamae–Brunhes geomagnetic reversal: decoupled thermal maximum and sea-level highstand during Marine Isotope Stage 19. Quat. Int. 383, 136–144.

Imbrie, J., Imbrie, J.Z., 1980. Modeling the climatic response to orbital variations. Science 207, 943–953.

Jicha, B.R., Singer, B.S., Sobol, P., 2016. Re-evaluation of the ages of ^{40}Ar/^{39}Ar sanidine standards and supereruptions in the western U.S. using a Noblesse multi-collector mass spectrometer. Chem. Geol. 431, 54–66.

Jouzel, J., Masson-Delmotte, V., Cattani, O., Dreyfus, G., Falourd, S., Hoffmann, G., Minster, B., Nouet, J., Barnola, J.-M., Blunier, T., Chappellaz, J., Fischer, H., Gallet, J.C., Johnsen, S., Leuenberger, M., Loulergue, L., Luethi, D., Oerter, H., Parrenin, F., Raisbeck, G., Raynaud, D., Schilt, A., Schwander, J., Delmo, E., Souchez, R., Spahni,

R., Stauffer, B., Steffensen, J.P., Stenni, B., Stocker, T.F., Tison, J.L., Werner, M., Wolff, E., 2007. Orbital and millennial Antarctic climate variability over the past 800000 years. Science 317, 793–796. http://dx.doi.org/10.1126/science.1141038.

Knudsen, M.F., Henderson, G.M., Frank, M., Mac Niocaill, C., Kubik, P.W., 2008. In-phase anomalies in beryllium-10 production and palaeomagnetic field behaviour during the Iceland Basin geomagnetic excursion. Earth Planet. Sci. Lett. 265 (3–4), 588–599. http://dx.doi.org/10.1016/j.epsl.2007.10.051.

Korschinek, G., Bergmaier, A., Faestermann, T., Gerstmann, U.C., Knie, K., Rugel, G., Wallner, A., Dillmann, I., Dollinger, G., Lierse von Gostomski, Ch., Kossert, K., Maiti, M., Poutivtsev, M., Remmert, A., 2010. A new value for the half-life of ^{10}Be by Heavy-Ion Elastic Recoil Detection and liquid scintillation counting. Nucl. Instrum. Methods Phys. Res., Sect. B, Beam Interact. Mater. Atoms 268 (2), 187–191. http://dx.doi.org/10.1016/j.nimb.2009.09.020.

Lal, D., Peters, B., 1967. Cosmic Ray Produced Radioactivity on the Earth. Handbuch der Physik, vol. XLVI/2. Springer, New York, pp. 551–612.

Laskar, J., Robutel, P., Joutel, F., Gastineau, M., Correia, A.C.M., Levrard, B., 2004. A long termnumerical solution for the insolation quantities of the Earth. Astron. Astrophys. 428, 261–285. http://dx.doi.org/10.1051/0004-6361:20041335.

Lisiecki, L.E., Raymo, M.E., 2005. A Pliocene–Pleistocene stack of 57 globally distributed benthic δ^{18}O record. Paleoceanography 20, 1–17. http://dx.doi.org/10.1029/2004PA001071.

Lisiecki, L.E., Stern, J.V., 2016. Regional and global benthic δ^{18}O stacks for the last glacial cycle. Paleoceanography 31. http://dx.doi.org/10.1002/2016PA003002.

Lourens, L.J., 2004. Revised tuning of Ocean Drilling Program Site 964 and KC01B (Mediterranean) and implications for the δ^{18}O, tephra, calcareous nannofossil, and geomagnetic reversal chronologies of the past 1.1 Myr. Paleoceanography 19, PA3010.

Maiorano, P., Capotondi, L., Ciaranfi, N., Girone, A., Lirer, F., Marino, M., Pelosi, N., Petrosino, P., Piscitelli, A., 2010. Vrica-Crotone and Montalbano Jonico sections: a potential unit-stratotype of the Calabrian Stage. Episodes 33, 218–233.

Maiorano, P., Bertini, A., Capolongo, D., Eramo, G., Gallicchio, S., Girone, A., Pinto, D., Toti, F., Ventruti, G., Marino, M., 2016. Climate signatures through the Marine Isotope Stage 19 in the Montalbano Jonico section (Southern Italy): a land-sea perspective. Palaeogeogr. Palaeoclimatol. Palaeoecol. 461, 341–361.

Marino, M., Bertini, A., Ciaranfi, N., Aiello, G., Barra, D., Gallicchio, S., Girone, A., La Perna, R., Lirer, F., Maiorano, P., Petrosino, P., Toti, F., 2015. Paleoenvironmental and climatostratigraphic insights for Marine Isotope Stage 19 (Pleistocene) at the Montalbano Jonico section, South Italy. Quat. Int. 383, 104–115. http://dx.doi.org/10.1016/j.quaint.2015.01.043.

Masarik, J., Beer, J., 2009. An updated simulation of particle fluxes and cosmogenic nuclide production in the Earth's atmosphere. J. Geophys. Res. 114, D11103. http://dx.doi.org/10.1029/2008JD010557.

Ménabréaz, L., Bourlès, D.L., Thouveny, N., 2012. Amplitude and timing of the Laschamp geomagnetic dipole low from the global atmospheric ^{10}Be overproduction: contribution of authigenic ^{10}Be/^{9}Be ratios in west equatorial Pacific sediments. J. Geophys. Res. 117 (B11101). http://dx.doi.org/10.1029/2012JB009256.

Ménabréaz, L., Thouveny, N., Bourlès, D.L., Vidal, L., 2014. The geomagnetic dipole moment variation between 250 and 800 ka BP reconstructed from the authigenic ^{10}Be/^{9}Be signature in West Equatorial Pacific sediments. Earth Planet. Sci. Lett. 385, 190–205. http://dx.doi.org/10.1016/j.epsl.2013.10.037.

Muscheler, R., Beer, J., Kubik, P.W., Synal, H.A., 2005. Geomagnetic field intensity during the last 60,000 years based on ^{10}Be and ^{36}Cl from the Summit ice cores and ^{14}C. Quat. Sci. Rev. 24 (16–17), 1849–1860.

Niespolo, E.M., Rutte, D., Deino, A.L., Renne, P.R., 2016. Intercalibration and age of the Alder Creek sanidine ^{40}Ar/^{39}Ar standard. Quat. Geochronol. http://dx.doi.org/10.1016/j.quageo.2016.09.004.

Petrosino, P., Jicha, B.R., Mazzeo, F.C., Ciaranfi, N., Girone, A., Maiorano, P., Marino, M., 2015. The Montalbano Jonico marine succession: an archive for distal tephra layers at the Early–Middle Pleistocene boundary in southern Italy. Quat. Int. 383, 89–103.

Pol, K., Masson-Delmotte, V., Johnsen, S., Bigler, M., Cattani, O., Durand, G., Falourd, S., Jouzel, J., Minster, B., Parrenin, F., Ritz, C., Steen-Larsen, H.C., Stenni, B., 2010. New MIS 19 EPICA Dome C high resolution deuterium data: hints for a problematic preservation of climate variability at sub-millennial scale in the "oldest ice". Earth Planet. Sci. Lett. 298, 95–103.

Raisbeck, G.M., Yiou, F., Cattani, O., Jouzel, J., 2006. ^{10}Be evidence for the Matuyama–Brunhes geomagnetic reversal in the EPICA Dome C ice core. Nature 444 (7115), 82–84. http://dx.doi.org/10.1038/nature05266.

Sánchez Goñi, M.F., Rodrigues, T., Hodell, D.A., Polanco-Martínez, J.M., Alonso-García, M., Hernández-Almeida, I., Desprat, S., Ferretti, P., 2016. Tropically-driven climate shifts in southwestern Europe during MIS 19, a low eccentricity interglacial. Earth Planet. Sci. Lett. 448, 81–93.

Sagnotti, L., Cascella, A., Ciaranfi, N., Macrì, P., Maiorano, P., Marino, M., Taddeucci, J., 2010. Rock magnetism and paleomagnetism of the Montalbano Jonico section (Italy): evidence for late diagenetic growth of greigite and implications for magnetostratigraphy. Geophys. J. Int. 180, 1049–1066.

Sagnotti, L., Giaccio, B., Liddicoat, J.C., Nomade, S., Renne, P.R., Scardia, G., Sprain, C.J., 2015. How fast was the Matuyama–Brunhes geomagnetic reversal? A new subcentennial record from the Sulmona Basin, central Italy. Geophys. J. Int. 204, 798–812.

Shackleton, N.J., Berger, A., Peltier, W.R., 1990. An alternative astronomical calibration of the lower Pleistocene timescale based on ODP Site 677. Trans. R. Soc. Edinb. Earth Sci. 81 (04), 251–261.

Siani, G., Sulpizio, R., Paterne, M., Sbrana, A., 2004. Tephrostratigraphy study for the last 18,000 14 C years in a deep-sea sediment sequence for the South Adriatic. Quat. Sci. Rev. 23, 2485–2500.

Simon, Q., Thouveny, N., Bourlès, D.L., Valet, J.-P., Bassinot, F., Ménabréaz, L., Guillou, V., Choy, S., Beaufort, L., 2016a. Authigenic ^{10}Be/^{9}Be ratio signatures of the cosmogenic nuclide production linked to geomagnetic dipole moment variation since the Brunhes/Matuyama boundary. J. Geophys. Res., Solid Earth 121. http://dx.doi.org/10.1002/2016JB013335.

Simon, Q., Thouveny, N., Bourlès, D.L., Nuttin, L., Hillaire-Marcel, C., St-Onge, G., 2016b. Authigenic ^{10}Be/^{9}Be ratios and ^{10}Be-fluxes (^{230}Th$_{xs}$-normalized) in central Baffin Bay sediments during the last glacial cycle: paleoenvironmental implications. Quat. Sci. Rev. 140, 142–162. http://dx.doi.org/10.1016/j.quascirev.2016.03.027.

Singer, B.S., 2014. A quaternary geomagnetic instability time scale. Quat. Geochronol. 21, 29–52.

Singer, B.S., Hoffman, K.A., Coe, R.S., Brown, L.L., Jicha, B.R., Pringle, M.S., Chauvin, A., 2005. Structural and temporal requirements for geomagnetic field reversal deduced from lava flows. Nature 434, 633–636.

Stefanelli, S., 2003. Benthic foraminiferal assemblages as tools for paleoenvironmental reconstruction of the Early–Middle Pleistocene Montalbano Jonico composite section. Boll. Soc. Paleontol. Ital. 42, 281–299.

Stefanelli, S., Capotondi, L., Ciaranfi, N., 2005. Foraminiferal record and environmental changes during the deposition of the Early–Middle Pleistocene sapropels in southern Italy. Palaeogeogr. Palaeoclimatol. Palaeoecol. 216, 27–52.

Suganuma, Y., Yokoyama, Y., Yamazaki, T., Kawamura, K., Horng, C.-S., Matsuzaki, H., 2010. ^{10}Be evidence for delayed acquisition of remanent magnetization in marine sediments: implication for a new age for the Matuyama–Brunhes boundary. Earth Planet. Sci. Lett. 296, 443–450. http://dx.doi.org/10.1016/j.epsl.2010.05.031.

Suganuma, Y., Okada, M., Horie, K., Kaiden, H., Takehara, M., Senda, R., Kimura, J.-I., Kawamura, K., Haneda, Y., Kazaoka, O., Head, M.J., 2015. Age of Matuyama–Brunhes boundary constrained by U–Pb zircon dating of a widespread tephra. Geology 43, 491–494. http://dx.doi.org/10.1130/G36625.1.

Tzedakis, P.C., Channell, J.E.T., Hodell, D.A., Kleiven, H.F., Skinner, L.C., 2012. Determining the natural length of the current interglacial. Nat. Geosci. 5, 138–141. http://dx.doi.org/10.1038/ngeo1358.

Valet, J.P., Fournier, A., Courtillot, V., Herrero-Bervera, E., 2012. Dynamical similarity of geomagnetic field reversals. Nature 490, 89–94. http://dx.doi.org/10.1038/nature11491.

Valet, J.P., Bassinot, F., Bouilloux, A., Bourlès, D.L., Nomade, S., Guillou, V., Lopes, F., Thouveny, N., Dewilde, F., 2014. Geomagnetic, cosmogenic and climatic changes across the last geomagnetic reversal from Equatorial Indian Ocean sediments. Earth Planet. Sci. Lett. 397, 67–79. http://dx.doi.org/10.1016/j.epsl.2014.03.053.

Valet, J.P., Meynadier, L., Simon, Q., Thouveny, N., 2016. When and why sediments fail to record the geomagnetic field during polarity reversals? Earth Planet. Sci. Lett. 453, 96–107.

Yin, Q., Berger, A., 2015. Interglacial analogues of the Holocene and its natural near future. Quat. Sci. Rev. 120, 28–46.